Birth sites of young stellar associations and recent star formation in a flocculent corrugated disc

Alice C. Quillen [ID],[1]⋆ Alex R. Pettitt [ID],[2] Sukanya Chakrabarti,[3,4] Yifan Zhang,[1] Jonathan Gagné[5,6] and Ivan Minchev [ID][7]

[1]*Department of Physics and Astronomy, University of Rochester, Rochester, NY 14627, USA*
[2]*Department of Physics, Faculty of Science, Hokkaido University, Sapporo 060-0810, Japan*
[3]*School of Physics and Astronomy, Rochester Institute of Technology, 84 Lomb Memorial Drive, Rochester, NY 14623, USA*
[4]*Institute for Advanced Study, Princeton, NJ 08540, USA*
[5]*Institut de Recherche sur les Exoplanètes, Université de Montréal, Pavillon Roger-Gaudry, PO Box 6128 Centre-Ville STN, Montréal QC H3C 3J7, Canada*
[6]*Planétarium Rio Tinto Alcan, Espace pour la Vie, 4801 av. Pierre-de Coubertin, Montréal, Québec, Canada*
[7]*Leibniz Institut für Astrophysik Potsdam (AIP), An der Sternwarte 16, D-14482, Potsdam, Germany*

ABSTRACT

With backwards orbit integration, we estimate birth locations of young stellar associations and moving groups identified in the solar neighbourhood that are younger than 70 Myr. The birth locations of most of these stellar associations are at a smaller galactocentric radius than the Sun, implying that their stars moved radially outwards after birth. Exceptions to this rule are the Argus and Octans associations, which formed outside the Sun's galactocentric radius. Variations in birth heights of the stellar associations suggest that they were born in a filamentary and corrugated disc of molecular clouds, similar to that inferred from the current filamentary molecular cloud distribution and dust extinction maps. Multiple spiral arm features with different but near corotation pattern speeds and at different heights could account for the stellar association birth sites. We find that the young stellar associations are located in between peaks in the radial/tangential (UV) stellar velocity distribution for stars in the solar neighbourhood. This would be expected if they were born in a spiral arm, which perturbs stellar orbits that cross it. In contrast, stellar associations seem to be located near peaks in the vertical phase-space distribution, suggesting that the gas in which stellar associations are born moves vertically together with the low-velocity dispersion disc stars.

Key words: Galaxy: disc – Galaxy: kinematics and dynamics – solar neighbourhood – open clusters and associations: general.

1 INTRODUCTION

Coeval groups of stars are tracers of the past sites of star formation in the Milky Way disc (e.g. Zuckerman & Song 2004). As it orbits the Galaxy, a recently formed cluster, group or association of stars, retains information on its birth location. However, birth locations are more uncertain for older clusters, due to uncertainties in the cluster age and in the galactic potential in which orbits are integrated (e.g. Dias et al. 2019). Close encounters with star clusters and molecular clouds, cluster evaporation, and non-axisymmetric and time-dependent gravitational forces associated with spiral arms, the Galactic bar, passage through the Galactic plane, and external tidal forces on the Galaxy disc perturb stellar orbits and increase the error in the estimated birth sites of stellar associations and clusters (e.g. Krause et al. 2020).

Because open clusters are expected to have predominantly been born in spiral arms, their orbits and ages have been used to probe the nature of spiral structure (Dias & Lepine 2005; Quillen et al. 2018a; Dias et al. 2019). The Lin-Shu hypothesis (Lin & Shu 1966; Shu 2016) posits that spiral structure is caused by density

waves moving through a galactic disc. The speed of the wave is described with an angular rotation rate called the pattern speed. In the 'modal' view of spiral structure, a single multi-armed wave with a constant pattern speed dominates (Lin & Shu 1966; Bertin et al. 1989; Shu 2016). A direct method for measuring the pattern speed of spiral arms relies on estimating the birth places of open clusters by integrating their orbits backwards (e.g. Dias & Lepine 2005; Naoz & Shaviv 2007; Dias et al. 2019). However, this method can give spurious results if spiral arms are not steady-state. Spiral arms could be transient (Toomre 1981; Sellwood & Carlberg 1984; Wada, Baba & Saitoh 2011; Grand, Kawata & Cropper 2012; Baba, Saitoh & Wada 2013; Baba et al. 2016), exhibiting variations in their amplitude, pitch angle, and pattern speed. Additional gravitational perturbations arise from the time-dependent and flocculent nature of the gas response (and hence that of the young stars) even when there is a time-steady spiral structure in the old stars (Chakrabarti, Laughlin & Shu 2003). Multiple patterns could simultaneously be present (e.g. Naoz & Shaviv 2007) and interfere (e.g. Quillen et al. 2011; Comparetta & Quillen 2012). External tidal perturbations on the Galaxy can induce spiral structure (e.g. Chakrabarti & Blitz 2009; Quillen et al. 2009; Dobbs & Pringle 2010; de la Vega et al. 2015; Pettitt et al. 2017). The recent study by Dias et al. (2019) mitigates the errors inherent in backwards orbit integration and

⋆ E-mail: alice.quillen@gmail.com

from assuming steady-state spiral structure by focusing on nearby (distances less than 5 kpc from the Sun) and younger than 50-Myr old open clusters with accurately measured distances, space motions, and ages.

Open clusters are groups of coeval stars, with most stars remaining in a gravitationally bound clump since birth. While they are not gravitationally bound entities, a number of moving groups and stellar associations seen in the solar neighbourhood also comprise coeval groups of stars (e.g. Eggen 1983; Zuckerman & Song 2004; Mamajek 2016; Riedel et al. 2017). Young stellar associations are predominantly identified in the solar neighbourhood (within about 150 pc of the Sun), and they span a range of ages, including some younger than 50 Myr. As most open clusters are more distant than the known young stellar associations (the open clusters studied by Dias et al. 2019 are within a few kpc from the Sun), stellar associations give a complimentary view of recent star formation near the Sun. We aim to probe the locations of spiral arm density peaks in the recent past by estimating the birth locations of coeval young stellar associations and moving groups.

Members of a young stellar association or young moving group in the solar neighbourhood share similar space velocities, or velocity components U, V, W, in heliocentric polar Galactic coordinates, with typical velocity dispersions below a few km s^{-1} (e.g. Binks, Jeffries & Maxted 2015; Mamajek 2016; Riedel et al. 2017; Gagné et al. 2018a). Young stellar associations are discovered by searching for nearby stars with similar proper motions and evidence of youth, with more detailed studies identifying additional members, confirming stellar association membership and finding substructures in the association age, velocity, and spatial distributions (e.g. Eggen 1983; de la Reza et al. 1989; de Zeeuw et al. 1999; Mamajek, Lawson & Feigelson 1999; Jayawardhana 2000; Binks et al. 2015; Mamajek 2016; Pecaut & Mamajek 2016; Gagné et al. 2018a, b; Gagné & Faherty 2018; Gagné, Faherty & Mamajek 2018c; Kos et al. 2019; Meingast, Alves & Furnkranz 2019; Binks et al. 2020; Tian 2020).

The brightest nearby young stars are not randomly distributed in the Galaxy (de Zeeuw et al. 1999; Elias, Alfaro & Cabrera-Cano 2006; Bouy & Alves 2015; Zari et al. 2018), rather those within 150 pc of the Sun appear to form a belt, known as the 'Gould belt', with an inclination of about 20° with respect to the Milky Way mid-plane (Herschel 1847; Gould 1874; Perrot & Grenier 2003). The Gould belt may be part of a larger vertical wavelike structure that is present in a filament of molecular cloud complexes (Zucker et al. 2020) dubbed the 'Radcliffe wave' (Alves et al. 2020). Vertical corrugations in molecular gas filaments could be related to the spiral seen in the distribution of solar neighbourhood stars in the vertical components of phase space z, $\dot{z}$ (Antoja et al. 2018). The dynamics of the interstellar medium differs from that of stars. Shocks and associated linear density enhancements in the gas can be caused by the spiral structure, whereas phase wrapping after a tidal perturbation (e.g. Minchev et al. 2009; de la Vega et al. 2015) in the vertical components of phase space (Candlish 2014; Antoja et al. 2018; Bland-Hawthorn et al. 2019) occurs in the stars but not in the gas and can persist in the phase-space structure of the stars for many crossing times. In contrast, density disturbances in the gas disc dissipate after a dynamical time. Prominent gas density perturbations in the Galaxy include the HI warp and planar disturbances (Levine, Blitz & Heiles 2006b, a). The height above or below the Galactic plane of birth sites of young stars may reflect the past location of features like the Gould belt and the Radcliffe wave. Vertical corrugations in the molecular disc and the stellar phase-space spiral are suspected to have been excited by tidal perturbations on the outer Galaxy (e.g. Chakrabarti & Blitz 2009; Quillen et al. 2009; Purcell et al.

2011; de la Vega et al. 2015; Antoja et al. 2018; Darling & Widrow 2019).

Structure in the distribution of VLBI observations of masers associated with high mass star formation regions (Xu et al. 2016, 2018; Reid et al. 2019) resembles that seen in extinction maps (Rezaei et al. 2018; Green et al. 2019; Lallement et al. 2019) and in a 3D map of nearby molecular clouds that is based on combining stellar photometric data with stellar *Gaia* DR2 parallax measurements to infer the distances of nearby dust clouds (Alves et al. 2020; Zucker et al. 2020). Spiral features seen in extinction maps (Quillen 2002; Rezaei et al. 2018; Green et al. 2019; Lallement et al. 2019), masers (Xu et al. 2016, 2018; Reid et al. 2019), and molecular clouds (Zucker et al. 2020) suggest that within a few kpc of the Sun, the Milky Way contains multiple spiral arms with morphology more flocculent than grand design. The recent open cluster study by Dias et al. (2019) matched open cluster birth locations to Perseus, Local and Sagittarius arms as traced by masers and H II regions and following logarithmic functions describing spiral arm peaks by Reid et al. (2014). The study of open cluster kinematics by Dias et al. (2019) found that these three spiral structures have pattern speeds nearly corotating with the Sun.

With the recent advances in identifying and characterizing young stellar associations (e.g. Malo et al. 2013; Riedel et al. 2017; Gagné et al. 2018a), it is a good time to look for connections between them and spiral arm candidates seen in the recently improved molecular cloud and extinction maps. To do this, we integrate the orbits of young stellar associations backwards to estimate their birth locations. We focus here on what we can learn from integrating the orbits of recent compilations of young stellar associations and star formation regions (e.g. Gagné et al. 2018a). Backwards orbit integration has been used to estimate kinematic ages of stellar associations by finding when their stellar members were likely to have been in proximity (de la Reza, Jilinski & Ortega 2006; Miret-Roig et al. 2018; Crundall et al. 2019). Here, we do not try to estimate kinematic ages, rather we search for patterns in the history of recent star formation near the Sun. We integrate orbits in three dimensions to probe the relation between birth heights, the corrugated molecular and dust disc, and patterns seen in the stellar vertical phase-space distribution (Antoja et al. 2018; Bland-Hawthorn et al. 2019; Laporte et al. 2019).

In Section 2, we specify coordinates, constants, and the potential model needed for orbit integration. The sample of stellar associations, clusters, and moving groups and their measurements are described in Section 3.

Results of backwards orbit integrations are discussed in Section 4.1. In Section 4.2, we discuss estimated stellar association birth locations in two dimensions. Birth heights above and below the plane are discussed in Section 4.3. In Sections 4.4 and 4.5, we look at birth sites in rotating frames and discuss possible molecular and extinction filaments that could be the current counterparts to past sites of star formation. In Sections 4.6 and 4.7, we compare stellar association phase-space coordinates to the distributions of stars in the solar neighbourhood. A summary and discussion follows in Section 5.

2 GALACTIC POTENTIAL MODEL FOR ORBIT INTEGRATION

We specify the Galactic coordinate systems and our notation for them in Section 2.1. We also review constraints on Galactic constants that are needed to carry out backwards orbit integrations. The gravitational potential we use to integrate the orbits is described in Section 2.2.

2.1 Coordinate system and Galactic constants

Numerous works have used the transformations given by Johnson & Soderblom ([1987](#)) to take stellar parallax, proper motion, position, and radial velocity measurements, and compute a heliocentric coordinate (x_h, y_h, z_h) and velocity vector (U, V, W). A heliocentric right-handed Cartesian coordinate system with origin at the Sun has Galactic coordinates

$$(x_h, y_h, z_h) = d(\cos b \cos l, \cos b \sin l, \sin b), \tag{1}$$

where b, l are Galactic latitude and longitude, respectively, and d is the distance of the point from the Sun. The positive z_h axis is along the north Galactic pole. Longitude $l = 0$, latitude $b = 0$, and small positive x_h correspond to a point that is closer to the Galactic Centre than the Sun. Galactic longitude $l = \pi/2$ and latitude $b = 0$ give positive y_h axis pointing in the direction of Galactic rotation. Heliocentric U, V, W velocity components are in cylindrical coordinates with U the radial component of velocity, V the tangential component, and W the vertical velocity component. These velocity components are positive towards the Galactic Centre in the direction of Galactic rotation and in the direction of the North Galactic pole. The velocities are in a heliocentric frame and so must be corrected for the solar motion with respect to the local standard of rest (LSR).

The galactocentric Cartesian coordinate system (x_g, y_g, z_g) has origin at the Galactic Centre. We compute galactocentric Cartesian coordinates (x_g, y_g, z_g) from heliocentric (x_h, y_h, z_h) Cartesian coordinates with

$$(x_g, y_g, z_g) = (-R_\odot + x_h, y_h, z_h + z_\odot), \tag{2}$$

where $z_\odot$ is the location of the Sun above or below the Galactic plane and $R_\odot$ is the galactocentric radius of the Sun. Based on trigonometric parallaxes of high-mass star-forming regions, Reid et al. ([2019](#)) find

$$z_\odot = 5.5 \pm 5.8 \text{ pc}, \tag{3}$$

which agrees with that found by Anderson et al. ([2019](#)) based on positions of H II regions. We adopt the value of $z_\odot = 5.5$ pc in our orbit integrations. However, we note that Bennett & Bovy ([2019](#)) find that $z_\odot = 20.8 \pm 0.3$ pc from measurements of the vertical stellar distribution function. In this galactocentric coordinate system, Galactic rotation in the x_g, y_g plane is clockwise about the origin. Galactocentric cylindrical coordinates R_g, θ_g, z_g can be computed using galactocentric azimuthal angle and radius

$$\theta_g = \text{atan2}(y_g, x_g), \qquad R_g = \sqrt{x_g^2 + y_g^2}. \tag{4}$$

The galactocentric azimuthal angle of the Sun, $\theta_\odot = \pi$, and the LSR has clockwise rotation with angular rotation rate $\dot{\theta}_g < 0$. A point with radius $R_g = R_\odot$ and small and negative $\theta - \theta_\odot$ is in front of the LSR in the direction of rotation.

From heliocentric U, V, W velocity components, we compute the galactocentric velocity in cylindrical coordinates

$$(v_R, v_\theta, v_z) = (-(U + U_\odot), -(V + V_\odot + V_{LSR}), W + W_\odot), \tag{5}$$

where $(U_\odot, V_\odot, W_\odot)$ is the peculiar velocity of the Sun in cylindrical coordinates with respect to the LSR. For this velocity transformation, we adopt a peculiar solar motion of

$$(U_\odot, V_\odot, W_\odot) = (11.1^{+0.69}_{-0.75}, 12.24^{+0.47}_{-0.47}, 7.25^{+0.37}_{-0.36}) \text{ km s}^{-1} \tag{6}$$

based on an analysis of local stellar kinematics (Schönrich, Binney & Dehnen [2010](#)).

Using the pericenter passage of a star around the Galaxy's central supermassive black hole, the GRAVITY Collaboration ([2018](#))

measures the galactocentric radius of the Sun

$$R_\odot = 8.122 \pm 0.031 \text{ kpc}. \tag{7}$$

This radius, the proper motion of the radio source associated with the Galaxy's central black hole, Sgr A∗, and the tangential component of the solar peculiar motion measured by Schönrich et al. ([2010](#)) give LSR rotational velocity (and following section 8.2 by Reid et al. [2019](#))

$$V_{LSR} = 233 \pm 1.4 \text{ km s}^{-1}. \tag{8}$$

These values are consistent with those computed from trigonometric parallaxes of high-mass star formation regions (Reid et al. [2019](#)) and we use these values in our orbit integrations. These values give LSR angular rotation rate $\Omega_\odot = V_{LSR}/R_\odot = 28.7$ km s^{-1} kpc^{-1}.

2.2 The Galactic potential and backwards orbit integration

The stars in young stellar associations are in nearly circular orbits that remain within 150 pc of the Galactic plane. Rather than use a mass model for the entire galaxy comprising disc, bulge, and halo components (e.g. Robin et al. [2003](#); Deg et al. [2019](#)), we use a local axisymmetric potential model that matches the slope of the rotation curve near the Sun's galactocentric radius and measurements of the vertical acceleration of stars above the Galactic plane. A multiple mass component Milky Way model is not needed as we integrate only low eccentricity and low inclination orbits. In cylindrical coordinates, we approximate the potential as

$$\Phi(R_g, z_g) = \Phi_R(R_g) + \Phi_z(z_g). \tag{9}$$

As did Darling & Widrow ([2019](#)), we adopt a static, axisymmetric potential function that is separable in the radial and vertical coordinates.

We describe the slope of the Galactic rotation curve with an exponent β (following Dehnen [1999](#), Appendix B). The tangential velocity of a star in a circular orbit in the Galactic plane

$$v_c(R_g) = \begin{cases} V_{LSR} & \text{for } \beta = 0 \\ V_{LSR} \left(\dfrac{R_g}{R_\odot} \right)^\beta & \text{for } \beta \neq 0 \end{cases}. \tag{10}$$

For this power-law rotation curve, the radius of a circular orbit with z component of angular momentum L is

$$R_L(L) = R_\odot \left(\frac{L}{R_\odot V_{LSR}} \right)^{\frac{1}{1+\beta}} \tag{11}$$

(Dehnen [1999](#)). The rotation curve (equation 10) is consistent with radial potential function

$$\Phi_R(R_g) = \begin{cases} V_{LSR}^2 \ln \left(\dfrac{R_g}{R_\odot} \right) & \text{for } \beta = 0 \\ \dfrac{V_{LSR}^2}{2\beta} \left(\dfrac{R_g}{R_\odot} \right)^{2\beta} & \text{for } \beta \neq 0. \end{cases} \tag{12}$$

With a mass model and terminal velocity constraints based on observations of atomic and molecular gas emission lines, McGaugh ([2019](#)) estimates a rotation curve slope at the solar galactocentric radius $R_\odot$ of

$$\left. \frac{dv_c(R_g)}{dR_g} \right|_{R_\odot} = -1.7 \pm 0.1 \text{ km s}^{-1} \text{ kpc}^{-1}. \tag{13}$$

This slope is the same as the one inferred from recent measurements of Oort's A and B constants (Li, Zhao & Yang [2019](#)) and is similar

to the slope

$$\frac{dv_c(R_g)}{dR_g}\bigg|_{R_\odot} = -1.34 \pm 0.21 \ \text{km s}^{-1} \ \text{kpc}^{-1} \tag{14}$$

measured from Cepheids (Mróz et al. 2019). The slope is related to the slope exponent

$$\beta = \frac{dv_c}{dR_g}\bigg|_{R_\odot} \frac{R_\odot}{V_{LSR}} = \frac{dv_c}{dR_g}\bigg|_{R_\odot} \frac{1}{\Omega_\odot}. \tag{15}$$

Using $R_\odot = 8.12$ kpc and $V_{LSR} = 233.3$ km s^{-1}, the slopes by McGaugh (2019) and Li et al. (2019) give $\beta = -0.059$ whereas the slope by Mróz et al. (2019) gives $\beta = -0.045$. The slope by McGaugh (2019) is measured in the range $9 < R_g < 19$ kpc whereas that by Mróz et al. (2019) is for $4 < R_g < 20$ kpc. The slope by Li et al. (2019) is based on stars in the solar neighbourhood. We adopt $\beta = -0.05$ as a compromise.

The sensitivity of the gravitational potential to height above or below the Galactic plane, z_g, depends on the density distributions in thick and thin stellar discs, gas disc, and halo. The recent local 3D models (Barros, Lépine & Dias 2016) are based on measurements for the different galactic components (Holmberg & Flynn 2000, 2004; Flynn et al. 2006). We fit simple analytical functions to the vertical acceleration as a function of height above the Galactic plane found from solar neighbourhood K-giants that is shown in fig. 8 by Holmberg & Flynn (2004). We found a good fit to this curve within $z_g < 750$ pc with a polynomial function

$$\ddot{z}_g = -\frac{d\Phi_z(z_g)}{dz_g} = -\alpha_1 z_g - \alpha_2 z_g^2 \text{sign}(z_g), \tag{16}$$

with constants

$$\alpha_1 = 4207.0 \ \text{Gyr}^{-2} \tag{17}$$

$$\alpha_2 = -2792.2 \ \text{Gyr}^{-2} \ \text{kpc}^{-1}. \tag{18}$$

This vertical acceleration is derived from a vertical potential function

$$\Phi_z(z_g) = \frac{1}{2}\alpha_1 z_g^2 + \frac{1}{3}\alpha_2|z_g|^3 + \text{constant.} \tag{19}$$

Poisson's equation applied in the mid-plane at $R_\odot$ gives a value for the frequency of low-amplitude vertical oscillations,

$$\nu^2 = \frac{d^2\Phi_z(z_g)}{dz_g^2}\bigg|_{z_g=0} = 4\pi G\rho_0 - 2\beta\Omega_\odot^2, \tag{20}$$

where ρ_0 is the mid-plane mass density and we have used the potential of equation 12 for the radial derivative terms. The estimated value for the mid-plane density near the Sun is $\rho_0 = 0.10 \, M_\odot \text{pc}^{-3}$ (Holmberg & Flynn 2004). This value is comparable to the value for the local density of matter found in recent work (McKee, Parravano & Hollenbach 2015), which includes the density of visible stars (with improvements to prior work particularly for the density of M dwarfs and white dwarfs), the gas density, and the inferred dark matter density. Using our adopted value for $\Omega_\odot$ and this mid-plane density, the frequency of low-amplitude vertical oscillations $\nu \approx 0.076$ rad Myr^{-1} and the period of vertical oscillations is 83 Myr. The frequency of oscillations computed using α_1 is somewhat lower, $\nu = \sqrt{\alpha_1} = 0.065$ rad Myr^{-1}. These frequencies are lower than that used by Candlish (2014) whose Galactic models have $\nu \approx 0.095$ rad Myr^{-1} near the mid-plane (see their fig. 6). We attribute the discrepancies to the different conventions adopted for $R_\odot$ and V_{LSR}.

Orbits are integrated backwards using the Galactic potential model of equations (9)–(18) and with PYTHON's general purpose

integration routine `odeint`, which calls the LSODA routine from the FORTRAN77 library `odepack`. Each orbit consists of a series of positions and velocities as a function of time t where $t = 0$ is the present and $t < 0$ corresponds to times in the past. We integrate multiple separate orbits for each stellar association, each with slightly different initial conditions. The initial conditions for each orbit are the mean estimated value of the stellar association central position x_h, y_h, z_h and velocity U, V, W plus randomly generated offsets in these six quantities that are based on estimates for the spatial extent and velocity dispersion of the association. The initial position and velocity offsets for integration are generated using a normal distribution and standard deviations σ_x, σ_y, σ_z, σ_U, σ_V, σ_W in the phase-space coordinates for each association. Because we desire estimates for both spatial extent and velocity dispersion of each association, we use measurements for stellar associations that are based on a multivariate fitting algorithm (Malo et al. 2013; Gagné et al. 2018a).

3 SAMPLE OF YOUNG STELLAR ASSOCIATIONS, CLUSTERS, AND MOVING GROUPS

Most of the young stellar associations, clusters, and moving groups we use for this study are taken from table 9 by Gagné et al. (2018a). This table lists values for central coordinates and velocities x_h, y_h, z_h, U, V, W and standard deviations for these quantities found using the BANYAN algorithm (Gagné et al. 2018a). BANYAN (Bayesian Analysis for Nearby Young AssociatioNs) models the distribution of stars in the young stellar associations with multivariate Gaussian distributions in six dimensional phase space. The standard deviations, σ_x, σ_y, σ_z, σ_U, σ_V, σ_W, reflect the spatial extent and velocity dispersions of the associations, not errors in measuring these quantities.

The longer orbits are integrated, the larger the errors in the orbit positions. To mitigate this uncertainty, we restrict our study to associations that are younger than 70 Myr. We have discarded the 118 Taurus group and the Platais 8 cluster (Platais, Kozhurina-Platais & van Leeuwen 1998) because they have been neglected in recent studies and the constraints on their ages are poor. To the associations listed by Gagné et al. (2018a), we add the Argus association but with measurements from the BANYAN analysis using the members and measurements by Zuckerman (2019) and a recently discovered $\approx$62-Myr-old stellar association, μ Tau (Gagné et al. in preparation). We have checked that the results of the BANYAN analyses by Gagné et al. (2018a) are consistent with the mean position and velocity measurements by other recent works (Binks et al. 2015; Riedel et al. 2017; Miret-Roig et al. 2018).

For some associations (e.g. those associated with the Scorpius–Centaurus OB association), more recent *Gaia*-based observations have improved upon central positions and velocity dispersion (e.g. Wright & Mamajek 2018) but have not fit the spatial extent of the association. We have adopted not to use these more precise measurements as there are correlations between the measured variables from the BANYAN analysis (Gagné et al. 2018a), and we would like to integrate multiple trial orbits for each association. Recent studies have uncovered additional substructure (in age, velocity, and position) in some star formation regions, such as Corona–Australis – (Galli et al. 2020), Taurus – (Fleming et al. 2020), Scorpius–Centaurus – (Pecaut & Mamajek 2016; Wright & Mamajek 2018), and Orion – (Kos et al. 2019; Tian 2020). Such substructure corresponds to gradients over small distances in the Galaxy compared to distances travelled since birth in the orbit. We ignore substructure

in the associations and star formation regions here but keep in mind that a fuller and more accurate picture of the pattern of star formation in the Galaxy might be sensitive to stellar association substructures.

The star formation regions, moving groups, open clusters and stellar associations used here, their abbreviations, and their measured ages t_{age}, are listed in Table 1. Standard deviations for the ages σ_{age} are estimated from the ranges and uncertainties given in the literature with citations for the age estimates also listed in this table. The central positions and velocities and the standard deviations from the BANYAN analyses are listed in Table 2.

The youngest associations are born in at least two different filamentary extinction and molecular cloud structures. The Scorpius–Centaurus star formation region includes the ρ Ophiucus star formation region (ROPH), the Upper Scorpius (USCO), Lower Centaurus Crux (LCC), and Upper Centaurus Lupus (UCL) groups that lie above the Galactic plane and connect to a molecular filament that contains the Aquila Rift molecular clouds (Bell, Mamajek & Naylor 2015; Mamajek 2016; Pecaut & Mamajek 2016) at Galactic longitude $l \sim 18°$ and a distance of $d \sim 200$ pc (Zucker et al. 2020). In contrast, the Taurus–Auriga star formation region (TAU) and 32 Orionis group (THOR) are below the Galactic plane and might instead be associated with the filament showing the Radcliffe wave that contains the Orion star formation region (Alves et al. 2020). Maps of the current locations of stellar associations are shown in figs 4 and 5 by Gagné et al. (2018a). We will discuss association locations in context with the extinction and molecular gas filaments in more detail in subsequent sections.

4 RESULTS

Using backwards orbit integration, we first look at stellar association birth sites in two dimensions or equivalently projected into the Galactic plane. In Section 4.3, we discuss birth heights above or below the Galactic plane. In Sections 4.4 and 4.5, we discuss the birth sites in rotating frames. In Sections 4.6 and 4.7, we discuss the stellar associations in context with the solar neighbourhood's stellar velocity and vertical phase-space distribution.

4.1 Estimated birth locations

Estimated birth locations and velocities computed from our orbit integrations, along with their uncertainties, are listed in Table 3. Birth height, galactocentric radius, azimuthal angle, z_b, R_b, $\theta_b - \theta_\odot$, and birth velocity components $v_{z,b}$, $v_{R,b}$ are mean values at the association age t_{age} of 30 integrated orbits with randomly generated initial conditions, chosen as described at the end of Section 2.2. We computed a standard deviation from the scatter of the values in the 30 orbits at t_{age}. We also computed a standard deviation from a single orbit by weighting points in the orbit with a factor that depends on the age uncertainty or spread

$$w(t) = \exp\left(-\frac{(|t| - t_{age})}{2\sigma_{age}^2}\right). \tag{21}$$

The uncertainties for birth positions and velocities listed in Table 3 are the result of summing these two estimated standard deviations in quadrature. Errors caused by the spread in initial conditions usually dominate those arising from the age uncertainty. We neglect errors in the orbits caused by uncertainty in astronomical constants $z_\odot$,

$R_\odot$, V_{LSR}, $U_\odot$, $V_\odot$, and $W_\odot$ and parameters describing the potential model, β, α_1, and α_2.

In Table 3, we also list the maximum height above or below the Galactic plane $|z|_{max}$ reached in the orbit. We measured these from the backwards orbit integrations by integrating longer than a full vertical oscillation period. This is a measure of the orbit's amplitude of vertical oscillations. The uncertainty is the standard deviation computed from the scatter in $|z|_{max}$ for 10 orbits with different initial conditions. We also computed and list a measure of the orbital eccentricity from the maximum and minimum radius reached in the orbit $e = \frac{R_{g,max} - R_{g,min}}{R_{g,max} + R_{g,min}}$, with uncertainty estimated the same way as for $|z|_{max}$. We also list the radius R_L of a planar circular orbit with the same z component of angular momentum computed using equation 11. As the potential is axisymmetric, the z component of angular momentum per unit mass, L, is a conserved quantity and depends only on an orbit's initial conditions. The standard deviation of R_L is computed by propagating the errors in the initial conditions. The birth tangential velocity component $v_{\theta,b}$ can be computed from R_L and birth radius R_b by inverting equation 11, giving $L = R_\odot V_{LSR} \left(\frac{R_L}{R_\odot}\right)^{\beta+1}$ and $v_{\theta,b} = L/R_b$.

Birth locations and velocities and maximum orbital height are plotted as a function of stellar association age in Fig. 1. In this plot, the vertical error bars are uncertainties due to the spread in the initial (and current) positions and velocities. Horizontal error bars show age spread or uncertainty. Horizontal coordinates are listed in Table 1 and vertical coordinates are listed in Table 3. In Fig. 1, the horizontal grey lines are at a vertical coordinate of zero except in the fourth panel where it is at the galactocentric radius of the Sun, $R_g = R_\odot$. The bottom panel in Fig. 1 shows the angle $\theta_b - \theta_\odot - |\Omega_\odot t_{age}|$ in degrees. This angle gives birth azimuthal angle in a frame corotating with the LSR. This angle is the difference between the birth angle θ_b and that of a particle in a circular orbit that is at the location of the Sun at $t = 0$.

Fig. 1 shows some trends with age. The youngest stellar associations are born both above and below the Galactic plane and are on nearly circular orbits. Intermediate age associations (20–30 Myr) have lower vertical amplitudes (lower $|z|_{max}$). The older associations are coming into the solar neighbourhood from both larger and smaller radii. These trends will be discussed in more detail below.

We have checked that variations in the adopted value of galactocentric solar radius $R_\odot$, LSR velocity V_{LSR} and rotation curve slope β, within the errors of recent measurements, do not significantly affect the morphology of the orbits in Figs 1 and 2 or trends discussed below. With a flat rotation curve, corresponding to exponent $\beta = 0$, the birth radii of the oldest associations would be at somewhat smaller (a few hundred pc lower) galactocentric radii.

4.2 Birth locations in the galaxy

In Fig. 2, we show the galactocentric radius and azimuthal angle $\theta_g - \theta_\odot$ for each of 10 orbits for each stellar association. The orbits of each association are shown in a different colour with colours identified in the key. At time t, the opacity of the point is weighted by the weight function $w(t)$ (equation 21), which peaks at 1 when time $|t|$ is the age of the association and has width dependent on the association age spread. This way points are visible only in the plot near the estimated association birth location. Points on the left side of the plot are older associations that were born further away from the Sun. The ages of these points can be estimated using the angular rotation rate of an object in a circular orbit at the galactocentric radius of the Sun (θ_g

Table 1. Stellar associations and moving groups, abbreviations, and ages.

Name	Abbreviation	Age (Myr)	σ_{age} (Myr)	Age reference
ρ Ophiucus star-forming region	ROPH	1	1	Wilking, Gagné & Allen (2008)
Taurus–Auriga star-forming region	TAU	1.5	1	Reipurth (2008)
ϵ Chamaeleontis association	EPSC	4	1	Murphy, Lawson & Bessell (2013)
Corona–Australis star-forming region	CRA	4.5	0.5	Gennaro, Moroni & Tognelli (2010)
TW Hydrae association	TWA	10	3	Bell et al. (2015)
Upper Scorpius group	USCO	10	3	Pecaut & Mamajek (2016)
Upper Corona–Australis association	UCRA	10	3	Gagné et al. (2018a)
η Chamaeleontis cluster	ETAC	11	3	Bell et al. (2015)
Lower Centaurus Crux group	LCC	15	3	Pecaut & Mamajek (2016)
Upper Centaurus Lupus group	UCL	16	2	Pecaut & Mamajek (2016)
32 Orionis group	THOR	22	4	Bell et al. (2015)
β Pictoris moving group	BPMG	24	3	Bell et al. (2015)
Octans association	OCT	35	5	Murphy & Lawson (2015)
Columba association	COL	42	5	Bell et al. (2015)
Argus association	ARG	45	5	Zuckerman (2019)
Carina association	CAR	45	8	Bell et al. (2015)
Tucana–Horologium association	THA	45	4	Bell et al. (2015)
IC2602 cluster	IC2602	46	5	Dobbie, Lodieu & Sharp (2010)
IC2391 cluster	IC2391	50	5	Barrado y Navascués, Stauffer & Jayawardhana (2004)
μ Taurus association	MTAU	62	10	Gagné et al. in preparation)

Notes. Standard deviations in age are estimated from the age range or uncertainty in age in the associated reference. Pecaut & Mamajek (2016) found a larger age spread of about 7 Myr in the Sco-Cen star formation regions. We adopted the age range of 3 Myr for UCRA and 10 Myr for MTAU as references lacked age range or error estimates. We adopted the age range for ETAC based on discussion by Bell et al. (2015), but also see Gennaro et al. (2010) and Murphy et al. (2013). For more discussion on ages and their errors and age distributions, see discussions by Riedel et al. (2017), Gagné et al. (2018a), references therein, and the references we have listed here.

Table 2. Central locations and variances from the BANYAN Gaussian models for the young stellar associations.

Name	Kin. ref.	x_h (pc)	y_h (pc)	z_h (pc)	U (km s^{-1})	V (km s^{-1})	W (km s^{-1})	σ_x (pc)	σ_y (pc)	σ_z (pc)	σ_U (km s^{-1})	σ_V (km s^{-1})	σ_W (km s^{-1})
ROPH	G18a	124.8	− 15.2	37.6	− 5.9	− 13.5	− 7.9	1.33	0.51	0.66	1.3	4.7	4.3
TAU	G18a	− 116.3	6.7	− 35.9	− 14.3	− 9.3	− 8.8	11.4	10.8	10.1	3.1	4.5	3.4
EPSC	G18a	49.9	− 84.8	− 25.6	− 9.9	− 19.3	− 9.7	2.5	3.6	4.0	1.6	2.2	2.0
CRA	G18a	132.4	− 0.2	− 42.4	− 3.7	− 15.7	− 8.8	3.71	0.75	2.04	1.3	2.2	2.2
TWA	G18a	14.4	− 47.7	22.7	− 11.6	− 17.9	− 5.6	12.2	9.7	3.9	1.8	1.8	1.6
USCO	G18a	121.2	− 17.0	48.9	− 4.9	− 14.2	− 6.5	17.0	8.2	8.9	3.7	3.2	2.3
UCRA	G18a	142.1	− 1.2	− 39.2	− 3.7	− 17.1	− 8.0	7.3	2.4	5.9	3.0	1.8	1.2
ETAC	G18a	33.6	− 81.4	− 34.8	− 10.0	− 22.3	− 11.7	0.65	0.98	0.71	1.6	2.8	1.8
LCC	G18a	54.3	− 94.2	5.8	− 7.8	− 21.5	− 6.2	11.9	12.4	13.7	2.7	3.8	1.8
UCL	G18a	107.5	− 60.9	26.5	− 4.7	− 19.7	− 5.2	21.0	19.6	13.5	3.8	3.0	1.7
THOR	G18a	− 88.4	25.7	− 23.9	− 12.8	− 18.8	− 9.0	4.1	6.9	5.1	2.2	2.2	2.0
BPMG	G18a	4.1	− 6.7	− 15.7	− 10.9	− 16.0	− 9.0	29.3	14.0	9.0	2.2	1.2	1.0
OCT	G18a	4.0	− 96.9	− 59.7	− 13.7	− 3.3	− 10.1	78.3	25.8	8.8	2.4	1.3	1.4
COL	G18a	− 25.9	− 25.9	− 21.4	− 11.9	− 21.3	− 5.7	12.1	23.0	17.8	1.04	1.29	0.75
ARG	Z19/G20	4.9	− 43.3	− 7.8	− 22.8	14.1	− 5.0	28.9	41.3	19.2	1.2	2.0	1.7
CAR	G18a	6.7	− 50.5	− 15.5	− 10.7	− 21.9	− 5.5	10.0	18.1	12.6	0.67	1.02	1.01
THA	G18a	5.4	− 20.1	− 36.1	− 9.8	− 20.9	− 1.0	19.4	12.4	3.8	0.87	0.79	0.72
IC2602	G18a	47.4	− 137.6	− 12.6	− 8.2	− 20.6	− 0.6	1.5	5.4	1.1	1.18	2.61	0.65
IC2391	G18a	1.9	− 148.1	− 18.0	− 23.0	− 14.9	− 5.5	1.3	6.4	1.4	1.10	3.40	0.78
MTAU	G20	− 130.7	0.2	− 79.7	− 14.2	− 24.2	− 6.2	21.9	20.8	12.4	3.0	1.7	2.4

Note. G18a = Gagné et al. (2018a); Z19 = Zuckerman (2019); and G20 = Gagné et al. (in preparation).

$-\theta_\odot)/\Omega_\odot$. This approximate age in Myr is shown with the top axis in Fig. 2.

The x-axis in Fig. 2, showing Galactic azimuthal angle, is reversed so that Galactic rotation is to the right. We chose this convention so that the plots can more easily be compared to maps of Milky Way spiral structure, extinction, and molecular clouds. The direction of Galactic rotation (clockwise) is shown with an arrow on the top right. The assumed galactocentric radius of the Sun is marked with a horizontal dotted grey line. The azimuthal angle of the Sun is marked with a dotted vertical line, so the current position of the Sun is on the right-hand side of the plot where the two dotted grey lines cross. In Fig. 2, increasing galactocentric R_g upward along the y-axis increases the heliocentric y_h coordinate. Moving to the right along the x-axis in Fig. 2 increases the heliocentric coordinate x_h.

Table 3. Birth sites and other orbital parameters for young stellar associations.

Name	z_b (pc)	$v_{z,b}$ (km s^{-1})	R_b (kpc)	$v_{R,b}$ (km s^{-1})	$\theta_b - \theta_\odot$ (rad)	R_L (kpc)	$\|z\|_{max}$ (pc)	Eccentricity
ROPH	44 ± 3	-0.5 ± 3.4	8.002 ± 0.004	-5.1 ± 1.0	0.031 ± 0.021	7.962 ± 0.185	56 ± 41	0.0228 ± 0.0070
TAU	-28 ± 13	-1.7 ± 3.6	8.234 ± 0.012	2.9 ± 3.7	0.042 ± 0.023	8.351 ± 0.124	52 ± 48	0.0281 ± 0.0072
EPSC	-10 ± 9	-2.7 ± 1.9	8.074 ± 0.005	0.4 ± 1.1	0.123 ± 0.026	7.849 ± 0.063	59 ± 23	0.0294 ± 0.0086
CRA	-29 ± 11	-2.2 ± 2.3	8.021 ± 0.008	-6.4 ± 1.4	0.129 ± 0.014	7.883 ± 0.070	41 ± 7	0.0331 ± 0.0075
TWA	7 ± 16	2.4 ± 1.1	8.087 ± 0.022	3.6 ± 2.1	0.287 ± 0.080	7.913 ± 0.061	42 ± 19	0.0239 ± 0.0038
USCO	37 ± 24	2.7 ± 2.1	8.056 ± 0.037	-4.6 ± 3.8	0.289 ± 0.081	7.927 ± 0.112	67 ± 11	0.0222 ± 0.0116
UCRA	-20 ± 11	-1.9 ± 0.8	8.038 ± 0.032	-4.1 ± 3.2	0.284 ± 0.080	7.803 ± 0.055	38 ± 7	0.0351 ± 0.0078
ETAC	23 ± 26	-4.6 ± 1.7	8.066 ± 0.021	5.1 ± 2.4	0.314 ± 0.078	7.736 ± 0.078	89 ± 25	0.0409 ± 0.0130
LCC	-7 ± 26	1.2 ± 1.2	8.057 ± 0.048	4.7 ± 3.9	0.427 ± 0.079	7.730 ± 0.109	37 ± 16	0.0462 ± 0.0099
UCL	-11 ± 26	2.8 ± 1.2	8.057 ± 0.061	1.2 ± 3.9	0.455 ± 0.053	7.749 ± 0.084	56 ± 14	0.0379 ± 0.0113
THOR	24 ± 33	-1.4 ± 0.7	8.094 ± 0.060	8.3 ± 2.7	0.618 ± 0.107	8.014 ± 0.072	53 ± 20	0.0296 ± 0.0108
BPMG	27 ± 13	-0.7 ± 0.6	8.065 ± 0.069	4.3 ± 2.4	0.683 ± 0.081	7.984 ± 0.063	28 ± 13	0.0171 ± 0.0035
OCT	69 ± 18	-1.0 ± 1.5	8.323 ± 0.127	-12.1 ± 1.9	1.041 ± 0.135	8.438 ± 0.104	69 ± 17	0.0361 ± 0.0056
COL	4 ± 17	-1.9 ± 0.8	7.773 ± 0.076	12.6 ± 1.7	1.201 ± 0.142	7.845 ± 0.040	24 ± 6	0.0424 ± 0.0058
ARG	-6 ± 19	-2.2 ± 1.2	9.026 ± 0.211	-38.4 ± 3.3	1.364 ± 0.123	9.034 ± 0.093	63 ± 28	0.1144 ± 0.0090
CAR	3 ± 18	-1.9 ± 1.1	7.704 ± 0.106	13.4 ± 1.9	1.293 ± 0.229	7.789 ± 0.036	31 ± 18	0.0440 ± 0.0033
THA	-1 ± 25	-6.6 ± 0.8	7.770 ± 0.059	12.3 ± 1.2	1.285 ± 0.114	7.809 ± 0.030	100 ± 12	0.0396 ± 0.0045
IC2602	-19 ± 30	-6.6 ± 0.8	7.767 ± 0.131	12.2 ± 3.5	1.330 ± 0.142	7.784 ± 0.087	105 ± 9	0.0384 ± 0.0112
IC2391	15 ± 8	-1.7 ± 0.8	7.742 ± 0.182	-3.1 ± 4.7	1.534 ± 0.148	8.055 ± 0.121	32 ± 9	0.0405 ± 0.0037
MTAU	64 ± 33	2.6 ± 2.5	7.461 ± 0.124	6.3 ± 5.5	1.828 ± 0.217	7.826 ± 0.066	81 ± 14	0.0509 ± 0.0084

Views of the integrated orbits plotted in 3D are shown in Fig. 3. We provide a supplemental movie **movie3D.gif** of the 3D plot seen at varying viewing elevations that is available online.

4.2.1 Inwards or outwards radial motion after birth

We find that most of the stellar associations have moved outwards radially from their birth locations. In other words, their current galactocentric radius exceeds their birth galactocentric radius. Exceptions to this trend are very young associations such as Corona Australius (CRA) and ρ Ophiucus (ROPH) associations that are still near their birth clouds. Among the older associations, the Octans (OCT) and Argus (ARG) associations have orbits that differ from the other associations. These two are also exceptions because they have moved inward to reach the solar neighbourhood since their birth.

As the rotation curve is nearly flat, the epicyclic frequency $\kappa \sim \sqrt{2}\Omega$ with Ω, the angular rotation rate of a particle in a planar circular orbit. This gives an epicyclic oscillation period of about 155 Myr at radius $R_\odot$. For the Argus and Octans associations, their ages correspond to only about a quarter of an epicyclic oscillation period. This implies that they must have been moving radially inward soon after birth, rather than outwards after birth as are most of the other associations.

The distance moved radially, or equivalently the epicyclic amplitude or orbital eccentricity, is largest for the LCC group and Argus (ARG) and μ-Taurus (MTAU) associations. If we assume that these associations were born in spiral arms, then the parent spiral features caused a greater degree of non-circular motion and so were probably more massive than the parent features of the youngest associations.

4.2.2 Expectations for inward or outward motion from models and simulations

Spiral features in *N*-body simulations usually show pattern speeds similar to or lower than the local angular rotation rate Ω (e.g. Quillen

et al. 2011; Grand et al. 2012; Kawata et al. 2014). Spiral arms in *N*-body simulations usually exhibit lower spiral pattern speeds at larger radii (e.g. Quillen et al. 2011; Grand et al. 2012; Kawata et al. 2014). As the Octans and Argus associations were born at larger Galactic radius, perhaps their birth arm had a slower pattern speed. The interstellar medium, with a sound speed similar to 10 km s^{-1}, is shocked as it passes over a spiral arm (e.g. Shetty et al. 2007; Dobbs & Pringle 2010; Pettitt et al. 2015; Shu 2016). The shock compresses the gas, increases the gas density, and lowers the gas velocity in the frame moving with the spiral pattern. The compressed gas should have an angular rotation rate that is approximately the same as that of the spiral pattern. In other words, in the frame moving with the spiral arm, the molecular clouds should have low angular rotation rate (e.g. Dobbs & Pringle 2010). Consider a star born with a low radial velocity component. If the star has an angular rotation rate that is slower than that of a particle in a circular orbit at the same radius, then its angular momentum is lower than that of the particle and it would move radially inward after birth. Perhaps the Octans and Argus associations were born in spiral features with pattern speeds that are lower than the angular rotation rate of a circular orbit, $|\Omega_s| < |\Omega|$, at their birth radius. The opposite could be true of most of the rest of the associations if $|\Omega_s| > |\Omega|$ for their birth spiral arm.

Dobbs & Pringle (2010) compared simulations of different galactic morphologies to assess their impact on the spread of cluster ages, inferred from the locations of densest gas elements (rather than a specific sub-grid star formation prescription). These models included a flocculent galaxy, a galaxy with a steady spiral, and a tidally perturbed galaxy. A steady spiral pattern shows a gradient in the ages of recently formed stars across each spiral arm. However, if star formation not only occurs along the arm, but in spurs and features emanating from the arm, the gradients are shallower. Spiral arms caused by tidal perturbations are more complex, exhibiting positive or negative age gradients across spiral arms. The simulated flocculent galaxy by Dobbs & Pringle (2010) shows localized bursts of star formation.
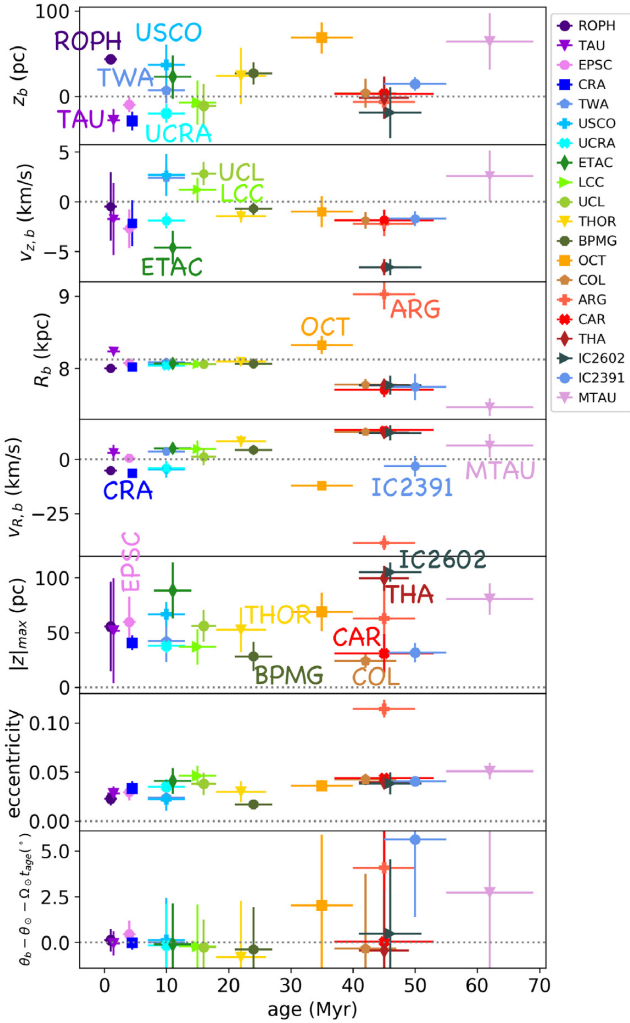
Figure 1. Birth locations and velocities of stellar associations plotted as a function of their age. Top to bottom panels show birth height z_b (in pc), vertical component of velocity at birth $v_{z,b}$ (in km s^{-1}), birth galactocentric radius R_b (in kpc), radial component of velocity at birth $v_{R,g}$ (in km s^{-1}), maximum height reached in the orbit $|z|_{max}$ (in pc), eccentricity, and angle in a frame rotating with the local standard of rest (in degrees). The y coordinates of points plotted here are listed in Table 3. The x coordinates are listed in Table 1. Vertical error bars are uncertainties due to spread in the initial coordinates and velocities. Horizontal error bars are uncertainties due to age spread or uncertainty.

Because there is no simple trend in age versus birth locations and kinematics (see also Fig. 1), continuous star formation without spurs or armlets along a single steady spiral arm seems ruled out. The other scenarios could be consistent with the stellar association birth locations and kinematics. Unfortunately, we have not found a study measuring young star epicyclic phases as a function of age from simulations (whether moving radially inward or outward), but perhaps this additional information could in future help differentiate between spiral structure models.

4.2.3 Location of stars after birth on leading or trailing sides of a parent spiral arm

To illustrate on which side of an arm stars would be located, we show in Fig. 4 a trailing logarithmic spiral arm in frames rotating

with the pattern speed of the arm. In Galaxies, the angular rotation rate is often higher at smaller radius than in the outskirts. A linear radial feature that winds up due to differential rotation would exhibit a 'trailing' spiral. Leading spiral features are probably rare (Buta, Byrd & Freeman 2003). Fig. 4(a) illustrates the case with arm pattern speed moving slower than the local rotation, $|\Omega_s| < |\Omega|$ and Fig. 4(b) illustrates the opposite case. In polar coordinates, a logarithmic spiral arm pattern can be described with peak at galactocentric radius $R_{peak}(\theta_g, t)$ where

$$\alpha_s \ln\left(\frac{R_{peak}(\theta_g, t)}{R_{s0}}\right) = \theta_g - \theta_\odot - \Omega_s t. \quad (22)$$

At time $t = 0$, the current time, the arm has a peak at galactocentric radius R_{s0} and at angle $\theta_\odot$. The arm pitch angle is $p = \arctan \alpha_s^{-1}$ and its pattern speed is Ω_s. As we have adopted a coordinate system giving clockwise Galactic rotation, $\dot\theta < 0$, a trailing arm has winding angle $\alpha_s > 0$. The pattern moves in the same sense as rotation, so the pattern speed $\Omega_s < 0$. A logarithmic trailing arm is linear on a plot of $\log R_g$ versus θ_g. The arm's pitch angle determines slope of the arm on this illustration with negative slope corresponding to a trailing arm.

In the illustration of Fig. 4, galactic rotation is to the right; however, in the rotating frame, stars move to the right in Fig. 4(a) and to the left in Fig. 4(b). With stars exceeding the pattern speed, as shown in Fig. 4(a), stars born on the arm pass the arm and are located to the right of the arm and near the direction of Galactic longitude $l \sim 90°$. With pattern speed exceeding that of a circular orbit, the pattern moves faster than the stars. In a frame rotating with the pattern, the arm is fixed and the stars move in the opposite direction and to the left, as shown in Fig. 4(b).

N-body simulations that exhibit spiral structures that are approximately corotating with the local angular rotation rate, $|\Omega_s| \sim |\Omega|$, have tangential peculiar velocities that are slower on the trailing side and faster on the leading side of a spiral arm and radial peculiar velocities that point outward on the trailing side and inward on the leading side (Grand et al. 2015; Baba et al. 2016). When its tangential velocity is slower than that of a circular orbit at the same radius, a star has lower angular momentum than the circular orbit and so must spend most of its orbit at lower radius. If the spiral pattern moves slower than the local angular rotation rate Ω, then the associations are currently found on the leading side of the arm, as shown in Fig. 4(b). Stellar associations with birth radius lower than their current values are consistent with the outward radial velocities and sub-circular birth tangential velocity reported in the simulations by Grand et al. (2015), on the trailing side of approximately corotating arms, if the spiral pattern speed is slightly higher than Ω. If the spiral arm or arms in which Octans and Argus associations formed have the opposite relation, $|\Omega_s| < |\Omega_\odot|$, then the associations are currently on the leading side of the arm and the trends noted by Grand et al. (2015) would be consistent with birth site exterior to $R_\odot$, as we have observed from their orbits.

4.2.4 Birth on leading or trailing sides of a spiral arm

Stars and gas in proximity to a spiral arm can gain or lose angular momentum due to the torque exerted by the gravitational pull of the spiral arm. When the spiral arm is approximately corotating with the galactic rotation, the change in angular momentum of nearby stars and gas clouds is larger because they remain on one side of the arm longer (e.g. Kawata et al. 2014). Stars and gas clouds trailing the arm, and stars born in these clouds, gain angular momentum and would then move outward in radius, whereas those leading the arm lose
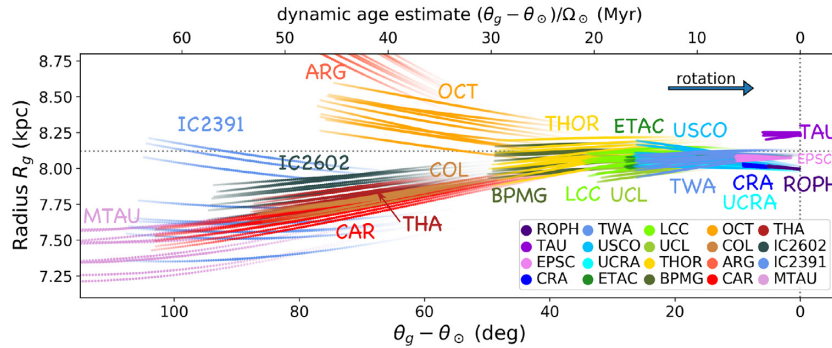
Figure 2. Backwards integration of young stellar associations younger than 70 Myr that are listed in Table 1. We plot orbits as a function of galactocentric radius and azimuthal angle from that of the Sun, $\theta - \theta_\odot$ in degrees. Ten orbits are shown for each stellar association to illustrate how the orbits depend upon the spread in initial conditions. Each stellar association is shown with a different colour point and the colours are labelled in the key. The opacity of the points is only high for points at times near the estimated stellar association birth age. Points on the left side of the plot are older associations that were born further away from the Sun. The ages of these points can be estimated using the angular rotation rate of an object in a circular orbit at the galactocentric radius of the Sun $(\theta_g - \theta_\odot)/\Omega_\odot$. This age coordinate is shown with the top axis. Associations were plotted in order of seniority, oldest ones first. Most of these associations were born at lower galactocentric radius and moved radially outward into the solar neighbourhood where they are found today. Dotted grey lines intersect at the location of the Sun and the direction of Galactic rotation is shown with an arrow. Note that the azimuthal angle increases to the left.
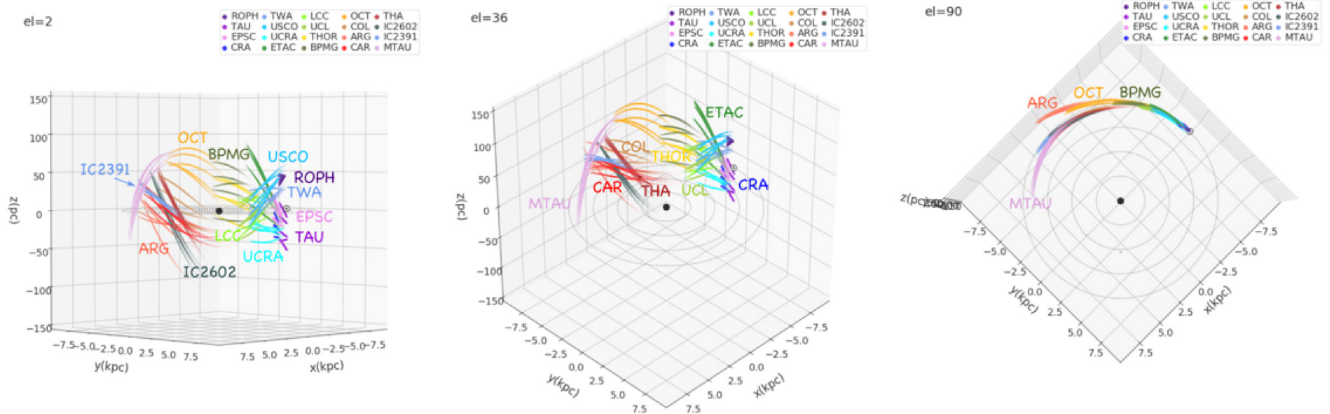
Figure 3. 3D plots of backwards orbit integrations. This figure is similar to Fig. 2 but five orbits are shown per stellar association. The Galactic Centre is the black dot. The position of the Sun is shown with a Sun symbol. The leftmost plot shows the heights of the backwards integrations whereas the rightmost plot shows the orbits projected on to the galaxy mid-plane. The central plot shows an intermediate view or viewing elevation. The viewing elevation is given in degrees on the top left. Note that the scale in *z* is not the same as that in *x, y*. We include a link to a supplemental movie that is available online **movie3D.mpg** of the 3D plot with a varying viewing angle.

angular angular momentum and would move inward (Kawata et al. 2014). An alternative explanation for the few associations that have moved radially inward after birth is that they were born on the leading side of a spiral arm that decreased their angular momentum rather than in a spiral arm that has a slower pattern speed than corotation. In this scenario, we might expect that stars are born on both leading and trailing sides of arms. If the Octans and Argus associations were born on the leading side of an arm, then we could look for stars that were born at the same time and in the same arm but on the trailing side. These would be moving outward from their birth site and so would not be near the Sun, but they might be near enough to find in a deeper survey of young stars. We estimate the birth galactocentric radius of the Octans association at 8.3 kpc, so trailing arm birth counterparts to the Octans association might be less than a kpc away from the Sun.

The youngest associations include Corona–Australis association (CRA) and ρ-Ophiucus star formation (ROPH) that are currently moving radially inward and were born moving radially inward. The Taurus–Auriga star forming region (TAU) is currently moving

outward and was born moving radially outward. However, it is unlikely that these were born on opposite sides of the same arm because they are still in proximity to their birth clouds and they are at different heights.

In summary, birth sites for most of the stellar associations are interior to the Sun's galactocentric radius and moved outward after birth. This would be consistent with birth in a spiral arm with pattern speed that is higher than $\Omega_\odot$ placing these associations currently on the leading side of their birth arm. This expectation follows from birth in a shock moving with the spiral arm and so with higher angular momentum than a circular orbit. The direction of motion is consistent with peculiar velocities seen in simulations of approximately corotating transient spiral structures by Grand et al. (2012). Alternatively, the associations that moved outward were born on the trailing side of a corotating spiral arm that increased their angular momentum through its gravitational torque (Kawata et al. 2014). The Octans and Argus associations are exceptions as they were born outside $R_\odot$ and this suggests that their parent spiral arm has a pattern speed slower than $\Omega_\odot$. Alternatively, they could have
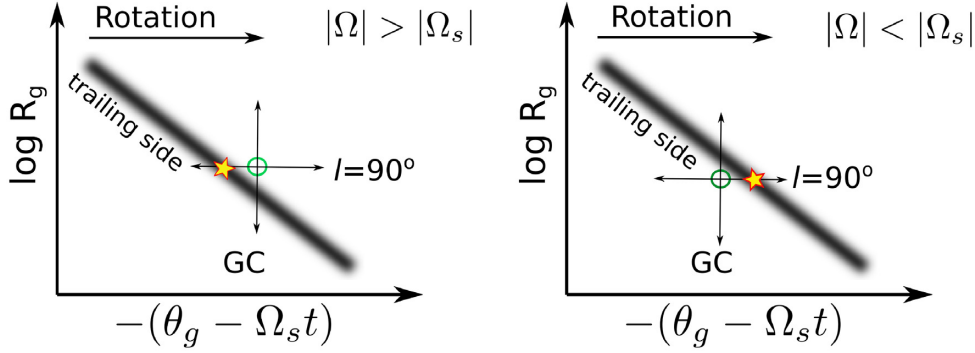
Figure 4. We illustrate a logarithmic spiral arm. Here, the *y*-axis is log galactocentric radius and the *x*-axis is galactic azimuthal angle in the frame moving with pattern speed of Ω_s. Clockwise galactic rotation is to the right and shown with the arrows on top. These arrows do not necessarily show the direction of motion in the rotating frame. We show a trailing logarithmic spiral arm (equation 22) with a wide diffuse black bar. The arm's pitch angle determines the slope of the bar with negative slope corresponding to a trailing arm. (a) If the angular rotation of a circular orbit is faster than the spiral pattern speed, $|\Omega| > |\Omega_s|$, stars born on the arm peak (shown as a yellow star) pass the spiral arm leaving them to the right of the spiral arm (shown as an open circle). If the Sun is located at the open circle, the four arrows show different viewing directions with Galactic longitude of 90° in the direction of rotation and GC representing towards the Galactic Centre. (b) If the angular rotation of a circular orbit is slower than the spiral pattern speed, $|\Omega| < |\Omega_s|$, stars born on the arm peak would move to the left of the arm.

been born on the leading side of a nearly corotating spiral feature and pulled inward by the arm itself (Kawata et al. 2014). Other scenarios, such as involving tidally excited spiral structure or spurs and armlets extending from strong arms, might also account for these inferences (e.g. Dobbs & Pringle 2010).

4.3 Birth heights

We examine the estimated stellar association birth heights listed in Table 3. Fig. 5(a) is similar to Fig. 2 and shows young stellar association orbits except that we only plot orbit points in different z_g ranges. Each panel corresponds to a planar slab with width 25 pc. The vertical slab upper and lower z_g values are labelled on each panel. Fig. 5(b) is similar to Fig. 5(a) except that *y*-axis in each panel is z_g and each panel shows only points in different ranges of galactocentric radius.

The intermediate-age associations (∼20 Myr) such as the β-Pictoris moving group (BPMG) and the 32 Orionis group (THOR) were born near the Galactic plane and at low eccentricity (also see Fig. 1). The Octans (OCT) and Argus (ARG) associations were probably born above the Galactic plane at larger radii than $R_\odot$. The Columba (COL), Tucana–Horologium (THA), and the Carina (CAR) associations were probably born near the Galactic plane. These inferences are based on a fixed and axisymmetric Galactic potential and so could be updated or corrected for orbits integrated in more complex potential models.

The birth locations of similar age associations that are at different heights are also at different radii and angles. The youngest associations can be divided into three groups: those at lower radius and above the Galactic plane (ROPH, USCO, TWA), those at lower radius and below the Galactic plane (CRA, UCL, LCC, UCRA), and those at larger radius and below the Galactic plane (TAU, EPSC). Fig. 5 does not necessarily imply that more than one molecular filament must exist simultaneously at the same R_g, θ_g but at different heights above or below the Galactic plane. Transitions in the birth sites of the different age associations seen in Fig. 5 suggest that there are spatial variations in the parent molecular cloud distribution. Recent star formation could have taken place in a corrugated molecular disc, as suggested by the current distribution of molecular clouds near the Sun (Alves et al. 2020; Zucker et al. 2020).

We have checked that the patterns shown in Fig. 5 are present with 20 per cent higher or lower values of parameter α_1, which we have used to describe the vertical acceleration in the Galaxy (see equation 16). Setting the height of the Sun $z_{g,\odot}$ to 20 pc does not significantly alter the overall appearance of the orbits.

Stars born above or below the Galactic plane, or with non-zero vertical velocity components, will undergo vertical oscillations. The maximum heights reached above or below the Galactic plane measured from the backwards orbit integration are listed in Table 3 and plotted as a function of stellar association age in the fourth panel of Fig. 1. The youngest stellar associations (less than 10 Myr old) have a range of maximum heights $|z|_{max} \sim 20$–60 pc (see Fig. 5b). However, the intermediate age association β Pictoris moving group (BPMG) and 32 Orionis (THOR) moving groups, with age ∼20 Myr, the Columba and Carina associations (COL and CAR; age ∼45 Myr), have lower vertical amplitudes less than 30 pc. The associations with the largest vertical amplitudes tend to be the older ones. The Octans and Argus associations (∼40 Myr old) that were born at larger radius have maximum heights in the range of 35–60 pc. The Tucana Horologium and μ Taurus associations (THA, MTAU) and IC2602 have the highest maximum heights in the range of 60–100 pc.

The wavelike or undulating structure seen in the filament of molecular clouds associated with the Local arm (Alves et al. 2020) could comprise clouds undergoing similar amplitude vertical motions but at different phases of oscillation. Alternatively, there might be spatial variations in the amplitudes of the vertical motions. The dip in the vertical amplitudes (the $|z_{max}|$-age plot in Fig. 1) of the intermediate age 32-Orionis and β Pictoris moving groups suggests that there are spatial variations in the vertical amplitudes of the parent molecular clouds. Tightly wound bending waves that travel through the disc (e.g. Hunter & Toomre 1969) would be expected to have amplitudes that are slowly varying with galactocentric radius and angle. In contrast, a phase wrapping model, where the Galactic disc was perturbed in the past and passively evolved afterward, could give a disc exhibiting variations in vertical amplitude over short distances (de la Vega et al. 2015). A tidal perturbation on the disc would excite stars in one region of the Galaxy more than other regions. Stars or gas clouds from different locations while the perturbation occured could be near the Sun now (e.g. Candlish 2014; de la Vega et al. 2015; Darling & Widrow 2019). An additional possibility is
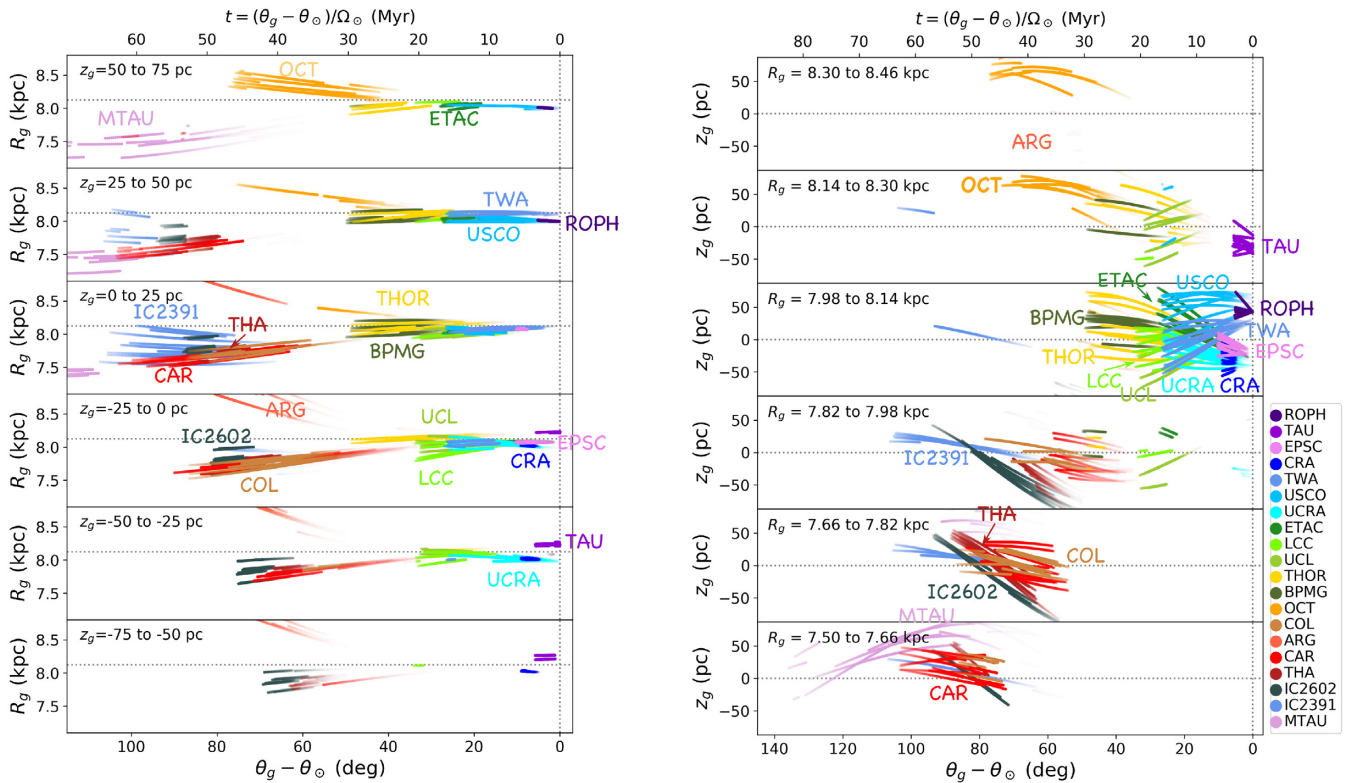
Figure 5. (a) Similar to Fig. 2 except that we plot galactocentric radius R_g versus angle for stellar association orbit positions that lie at different heights above or below the Galactic plane. Each panel corresponds to a different range of heights, and these are labelled on the top left of each panel. An orbit that varies in height would have points in more than one panel. (b) We plot height z_g versus angle and each panel plots only points in different ranges of galactocentric radii. The radial ranges are plotted on the top left of each panel. The older clusters are on the left and the younger ones on the right. These figures suggest that recent star formation has taken place in a corrugated molecular disc.

that these structures arise from orbits of stars moving in a dark matter halo that significantly departs from spherical symmetry due to past mergers with dwarf galaxies. However, it is likely that such an effect is minimal close to the mid-plane as prior work studying the evolution of halo shapes finds that baryonic-dominated regions are nearly spherical (Debattista et al. 2008; Prada et al. 2019).

In summary, trends in the birth heights of the stellar associations suggest that they were born in a corrugated disc of molecular clouds. Maximum vertical heights or vertical amplitudes reached above or below the galactic plane can be high (50–100 pc) for the youngest and oldest stellar associations but seem to be somewhat lower, only ∼30 pc for those 20–30 Myr old. This implies that there were spatial variations in the amplitudes of the vertical motions in the parent molecular cloud distributions.

4.4 Birth locations in rotating frames and birth spiral arm candidates

Keeping in mind that different associations were born at different heights, we now discuss orbits in different rotating frames. We explore the possibility that molecular cloud filaments near the Sun are spiral features, moving as waves, in which stellar associations were born.

In Fig. 6, we show backwards orbit integrations for the same sample of stellar associations as in Fig. 2; however, instead of plotting orbit positions at prior times t as a function of galactocentric angle, we plot association positions as a function of angle $\theta_g - \theta_\odot - \Omega_s t$ where Ω_s is an assumed pattern speed. Each panel shows the stellar

associations in a frame that is rotating with a different possible pattern speed. On the top axis, we show the distance along the solar circle, $R_\odot(\theta_g - \theta_\odot - \Omega_s t)$, to give a sense of scale for the x-axis. The y-axis is the natural log of galactocentric radius instead of radius but we have marked three values of radius in kpc on the right-hand side of the top panel to provide a sense of scale. A logarithmic spiral arm would be linear on Fig. 6. Trailing spiral arms should have a negative slope on these plots (as shown in Fig. 4).

In Fig. 6, extinction features, based on those labelled in 3D local extinction maps by Lallement et al. (2019), are plotted as grey bars. Molecular clouds are plotted as black dots using the data base by Zucker et al. (2020). Unfortunately, many of the masers identified in the feature called the 'Local Spur' at Galactic longitude $l \sim 50°$ by Xu et al. (2016, 2018) are further than 2 kpc away from the Sun and outside the region spanned by Fig. 6. The Local Spur may be connected to an extinction feature at $l \sim 50°$ and distance from the Sun $d < 500$ pc labelled as 'Vul' by Lallement et al. (2019) (see their fig. 14). A filament denoted the 'Split' by Lallement et al. (2019) contains the Serpens molecular clouds at longitude $l \sim 18°-30°$ and distance $d \sim 500–1200$ pc, the Aquila Rift at $l \sim 18°$ and a distance of $d \sim 200$ pc, and connects to the nearby Scorpius–Centaurus star formation region. The Vela C cloud at $l \sim 256°$ and $d \sim 900$ pc is also prominent in the extinction maps. The extinction filament associated with the Local Arm contains the Orion star formation region (at $l \sim 200°$ and $d \sim 400$ pc), Cepheus Near (at $l \sim 110°$ and $d \sim 340$ pc), North America (at $l \sim 84°$ and $d \sim 800$ pc), and Cygnus X clouds (at $l \sim 80°$ and $d \sim 1000$ pc). The longitudes and distances given here for these molecular clouds are based on those
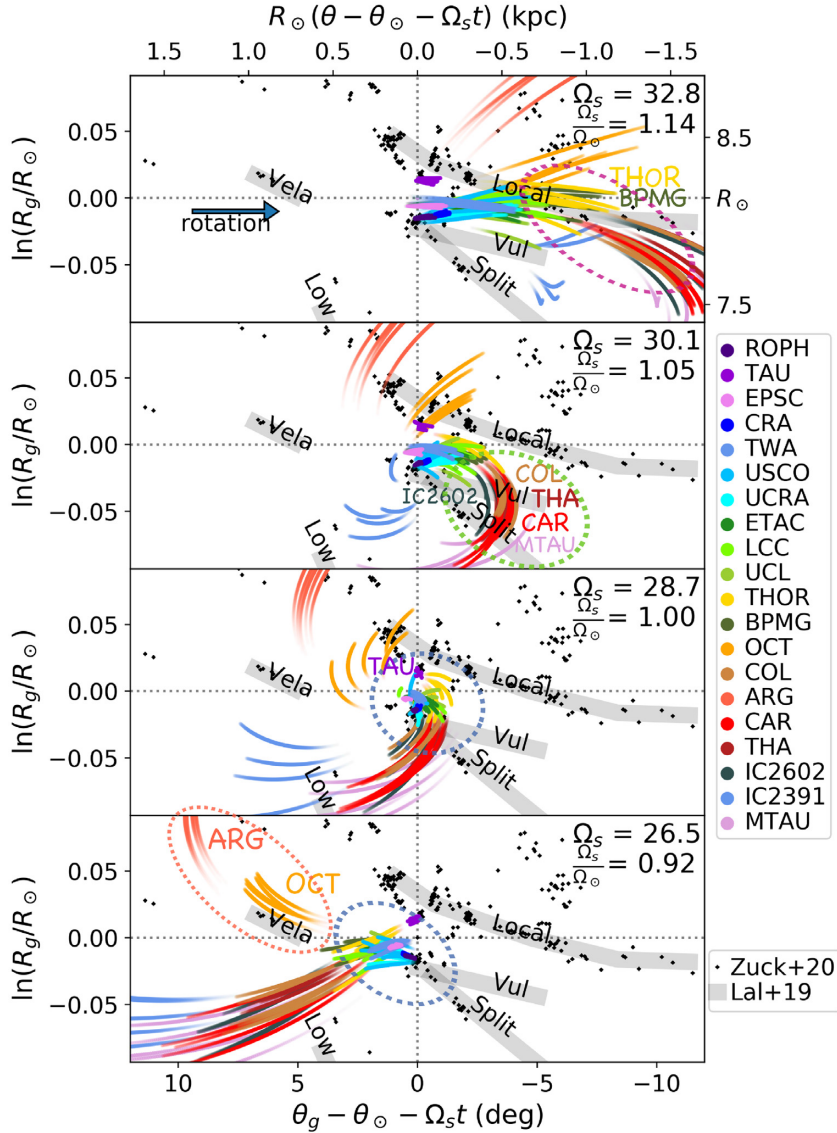
Figure 6. Backwards orbit integrations of young stellar associations plotted in rotating frames. Each panel is similar to Fig. 2 except that we plot galactocentric radius versus azimuthal angle in a frame rotating with a spiral arm pattern. The assumed pattern speeds for each panel are labelled on the top right of each panel in units of km s^{-1} kpc^{-1} and in units of $\Omega_\odot$. To give a sense of scale for the *x*-axis, the top axis shows distances in kpc along the solar circle of radius $R_\odot$. The *y*-axis is the natural log of galactocentric radius and we have marked three values of radius in kpc on the right-hand side of the top panel to provide a sense of scale. The third panel from the top has a corotating pattern speed, $\Omega_s = \Omega_\odot$. A spiral pattern near corotation allows the younger stellar associations to have been born in a compact region (marked with a dotted blue oval). If the pattern speed is near but below corotation (bottom panel, dotted blue oval), the young stellar associations could have been born on a continuation of the extinction feature known as the 'Split'. The Argus (ARG) and Octans (OCT) associations could have been born in a trailing filament with a lower pattern speed (the bottom panel, dotted orange oval). The Columba (COL), Tucana–Horologium (THA), Carina (CAR), μ-Taurus (MTAU) associations, and IC2602 cluster could have been born in a trailing filament with a faster pattern speed (see top two panels and the dotted green oval). If the pattern speed is as fast as $1.14\,\Omega_\odot$, the same feature could have been the birth site of the β Pictoris (BPMG) and 32 Orionis (THOR) moving groups (see the dotted pink oval in the top panel). No single pattern speed can account for all stellar associations.

listed in table A1 by Zucker et al. (2020). There is a nearby or lower component to the Sagittarius Carina arm denoted 'Low' in fig. 14 (for Lower Sagittarius Carina arm) by Lallement et al. (2019) that is approximately at $l \sim 330°$ and $d \sim 1$ kpc. These are the extinction features that are shown as grey bars and labelled on Fig. 6.

As discussed in Section 4.2.2, we suspect that associations that have moved radially outward after birth would have been born on spiral arms with pattern speed $|\Omega| < |\Omega_s|$ and they should be currently on the trailing side of their birth spiral arm. This implies that a counterpart to their birth arm would currently be located on the sky

in the direction of Galactic rotation or near Galactic longitude $l \sim 90°$ or on the right in Fig. 6. Candidates for the birth arm of the Octans and Argus associations, born with $R_g > R_\odot$, would be in the opposite direction, such as that associated with the Vela C cloud at $l = 265°$.

Can the Octans (OCT) and Argus (ARG) associations have been born on the same arm? If that arm has a faster pattern speed than $\Omega_\odot$, then a quite open rather than tightly wound arm would be required to parent both of these associations (see upper panels in Fig. 6). The Octans and Argus associations lie only on the same tightly

wound arm if that arm has a slower pattern speed, $|\Omega_s| \lesssim |\Omega_\odot|$ (see bottom panel of Fig. 6, and marked with a dotted orange oval), and agreeing with our discussion in Section 4.2. If the Vela C cloud is their parent filament, then its pattern speed $|\Omega_s| \sim 26.5\,\text{km s}^{-1}\,\text{kpc}$, which is lower than $\Omega_\odot$, as would be expected from the Octans and Argus association birth radii. We note that the birth filament could have been corrugated as the birth heights of the Octans and Argus associations differ ($z_b \sim 70, -6$ pc, respectively).

For the young associations (younger than 20 Myr old), candidates for the birth arm could be an extension of the local arm at Galactic longitude $l \sim 90°$ or the local spur at $l \sim 50°$ (connected to the extinction feature denoted 'Vul' here; Xu et al. 2018), or the extinction features denoted the 'Split' at $l \sim 30°$ (Lallement et al. 2019). If the pattern speed of the birth arm is near corotation $\Omega_s \approx \Omega_\odot = 28.7\,\text{km s}^{-1}\,\text{kpc}^{-1}$, then the associations were born in a compact region in the rotating frame (see the second panel from the bottom in Fig. 6 and dotted blue oval) but in between the Local arm and the Split. The near corotation pattern speed would support some recent estimates of local Galactic spiral pattern speeds (e.g. Naoz & Shaviv 2007; Dias et al. 2019). If the pattern speed was $|\Omega_s| \approx 26.5\,\text{km s}^{-1}\,\text{kpc}^{-1}$, then the young associations were born on a filament that is an extension of the 'Split' extinction feature. (Note that this slower pattern speed would contradict our expectation that associations that have moved outward after birth were born in faster pattern speed filaments.) The Taurus–Auriga star formation region could be associated with the Local arm rather than an extension of the Split; however, it is not at the same height as the clouds that appear nearest to it on Fig. 6 (this can be seen in Fig. 7).

With a faster pattern speed, $|\Omega_s| \sim 30\,\text{km s}^{-1}\,\text{kpc}$, as shown on the second from top panel of Fig. 6 (and marked with dotted green oval), many of the intermediate age associations (the Columba (COL), Tucana–Horologium (THA), Carina (CAR), μ-Taurus (MTAU) associations, and IC2602 cluster but not the IC 2391 cluster) could have been born in a single spiral feature. The faster pattern speed would be consistent with their lower birth radii. With a fast enough pattern (top panel), the youngest associations (less than 20 Myr old) are near a line with positive slope on Fig. 6 (in the top panel), corresponding to a leading rather than trailing pattern. This means that a filament with a fast pattern speed $|\Omega_s| \gtrsim 30\,\text{km s}^{-1}\,\text{kpc}$ is unlikely to have been the birth site of both the intermediate age associations (within the dotted pink oval on the top panel) and the youngest ones.

Spiral features in *N*-body simulations usually show pattern speeds similar to or lower than the local angular rotation rate Ω (e.g. Quillen et al. 2011; Grand et al. 2012; Kawata et al. 2014). Exceptions include spiral features that are driven by a bar (e.g. Lindblad, Lindblad & Athanassoula 1996) and spiral features that vary in pitch ange and strengthen due to interference between patterns (e.g. Quillen et al. 2011; Comparetta & Quillen 2012). Some models have a single feature that moves faster than local rotation at large radius but is below rotation at smaller radius (e.g. Sellwood & Carlberg 2014). A pattern with a fast pattern of $\Omega_s \approx \gtrsim 33\,\text{km s}^{-1}\,\text{kpc}$ would allow associations such as the β Pictoris (BPMG) and 32-Orionis (THOR) moving groups, the Columba (COL), Tucana–Horologium (THA), Carina (CAR), μ-Taurus (MTAU) associations, and the IC2602 cluster to be born on the same filament (Fig. 6 top panel). However, the birth radius of the 45-Myr-old Carina (CAR) and Tucana–Horologium (THA) associations is $R_b \sim 7.7$ kpc where the angular rotation rate $|\Omega| \sim 30.3\,\text{km s}^{-1}\,\text{kpc}$. The faster pattern speed of 33 km s^{-1} kpc exceeds the angular rotation rate of their birth radii. If their birth filament had such a fast pattern speed,

then the spiral arm dynamics would be in one of these exotic categories.

Fig. 6 implies that in the past 50 Myr, the pattern of spiral structure cannot be decomposed into a set of a few steady moving filaments. Transient behaviour and multiple molecular filaments seem necessary to explain even the most recent history of star formation near the Sun.

4.5 Heights in rotating frames

Using equation 20, the vertical oscillation period near the Sun is about 83 Myr. A quarter period is only 20 Myr. This implies that the stellar associations that are younger than 20 Myr right now have heights that are fairly near their birth heights. Likewise, their birth molecular cloud heights would not have changed significantly since their birth. This means that we can compare the past birth heights of the younger associations in rotating frames to the current positions of molecular clouds.

Fig. 7 is similar to Fig. 6 except that in each panel, we plot only positions that lie within specific planar slabs. The height ranges (in z_g) of each slab are printed on the top left of each panel. Each set of panels shows a single pattern speed, one just above $\Omega_\odot$ and the other just below $\Omega_\odot$.

In Fig. 7 left-hand panels, we show a pattern speed slightly below corotation. Because they are young, the positions of the youngest associations on this plot are not strongly sensitive to the pattern speed. Some groups related to the Scorpius Centaurus star formation region (USCO and ROPH) are above the Galactic plane and were born above the Galactic plane (see top panel in Fig. 1). There are some molecular clouds currently near their birth locations; however, there are more molecular clouds below the Galactic plane (see Fig. 7, left set of panels, green dotted oval). We had hoped to estimate how the height of a spiral feature varied in the last few million years, but these plots do not clearly pick out specific current molecular cloud counterparts for the different young stellar associations or a clear pattern of up and down motions in their star formation history. Most of the young stellar associations could have been formed on an arm that is a continuation of the 'Split' extinction feature, particularly if the pattern speed is slightly lower than corotation (see Fig. 7, left set of panels and as discussed in the previous section). We do not clearly see clear evidence for birth on different filaments at different radii and heights. The birth arm of the younger associations could have been thick, or contained sub-filaments at different heights or been so tightly corrugated that its history is not clearly visible in our plots.

On the right set of panels in Fig. 7, we show heights for a pattern speed slightly above corotation. The Columba (COL), Tucana–Horologium (THA), and Carina (CAR) associations have similar birth heights and locations in the rotating frame, so they could have been born on the same filament. These associations are about 40 Myr old, so their vertical height would have undergone half an oscillation period since birth. Their current (rather than birth) heights are near the Galactic plane. At their birth locations in the rotating frame, some of the clouds that are associated with the 'Split' extinction feature are also near the Galactic plane (see the second from bottom panel in Fig. 7, dotted brown ovals). This implies that these associations could have been born in an extension of the 'Split' extinction feature and their birth heights and the current heights of molecular clouds in this filament are approximately consistent with this scenario.
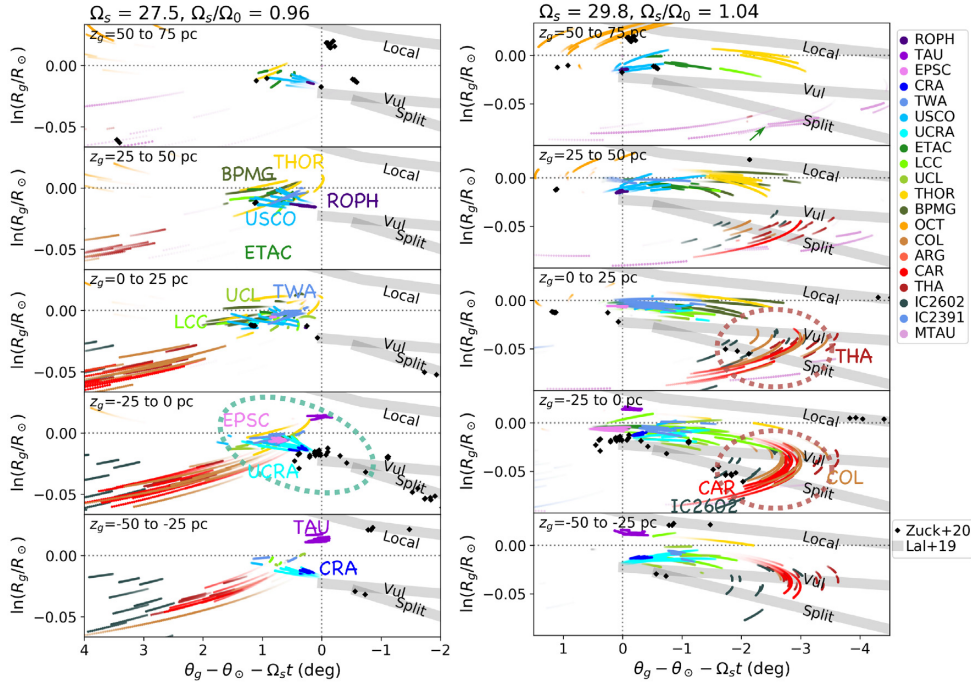
Figure 7. Orbits in rotating frames. Similar to Fig. 6 except each set of panels shows a single pattern speed and in each panel, we plot only positions that lie in a single planar slab. The range in height z_g is denoted on the top left of each panel. The assumed pattern speed Ω_s is written on the top of each set of panels in units of km s^{-1} kpc^{-1} and $\Omega_\odot$. The younger associations span a range of heights and are unlikely to have been born on a single corrugated filament. The birth arm of the younger associations could have been thick, or contained sub-filaments at different heights. The ϵ Chamaeleontis (EPSC) and Upper Corona–Australis (UCRA) associations have birth heights similar to that of a known filament of molecular clouds (see green dotted oval on the left set of panels) and could have been born on that filament it were approximately corotating with the local standard of rest. The Columba (COL), Tucana–Horologium (THA), and Carina (CAR) associations have similar birth heights and locations in a rotating frame (see brown dotted ovals on the right set of panels), so they could have been born on the same filament that is associated with the 'Split' or 'Vul' extinction features.

4.6 Stellar associations in comparison to the local velocity distribution

We discuss the stellar associations in context with the velocity distribution in the solar neighbourhood. In this section, we use the current, not birth, stellar association coordinates.

Quillen et al. (2018c) proposed that under-dense arcs in local velocity distributions separate stars that have recently crossed and been more strongly perturbed by a particular arm from those that have not. Since stellar associations could have been born in a nearby arm, we can test this hypothesis with them. They might be more likely to lie near the locus or underpopulated region in the velocity distribution. Stars on one side of the locus would not cross an arm, stars on the other side would cross it, and stars that graze the arm would lie on the locus. Stars born on the arm might be near or on the locus.

In Fig. 8, we show stellar association velocity components plotted as points on top of the velocity distribution (shown with a colour map) that is generated from nearby (within 200 pc) *Gaia* DR2 stars with radial velocity measurements (Gaia Collaboration 2018). The bottom two rows in Fig. 8 are similar to the top row except that only stars and associations above or below the plane are used to make the plot. This figure was generated with the same data base, selection criteria, and numerical scripts as the figures previously presented by Quillen et al. (2018c). The axes for the left-hand panels are galactocentric tangential and radial velocity components v_θ, $-v_r$ and those on the right-hand panels are v_θ and v_z. Each stellar association is plotted

with a different point shape but their colours and plotting order are the same as we have used in our previous figures.

Stellar associations are expected to have been born in spiral features. This implies that their current velocities should be on loci separating orbits that cross an arm from those that do not cross the same arm. Fig. 8 shows that the stellar associations studied here tend to be located between peaks in the local velocity distribution. The peak at $(v_\theta, v_r) \sim (220, 0)$ km s^{-1} is often called the Pleiades moving group or stream and that at $(v_\theta, v_r) \sim (240, 0)$ km s^{-1} often called the Coma Berenices moving group or stream (following the names used by Dehnen 1998). These streams contain stars with a wide range of ages (e.g. Dehnen 1998). The Coma Berenices moving group is more prominent in stars below the Galactic plane (Quillen et al. 2018b; Monari et al. 2018). The interpeak locations of the stellar associations on the v_θ, v_r velocity distribution is consistent with the hypothesis that dips in the velocity distribution are associated with orbits that touch nearby spiral density features.

Are the spiral patterns proposed by Quillen et al. (2018c) consistent with the stellar association locations on this plot? Only six patterns were shown (and listed in their table 1) and only two of them overlap with the galactocentric radius range covered by our Fig. 6. Because multiple features are probably required to account for the stellar associations birth sites (as discussed in Section 4.4), the model by Quillen et al. (2018c) is too simplistic to be predictive. The locus separating the Coma Berenices and Pleiades moving groups was connected to pericenter with an approximately
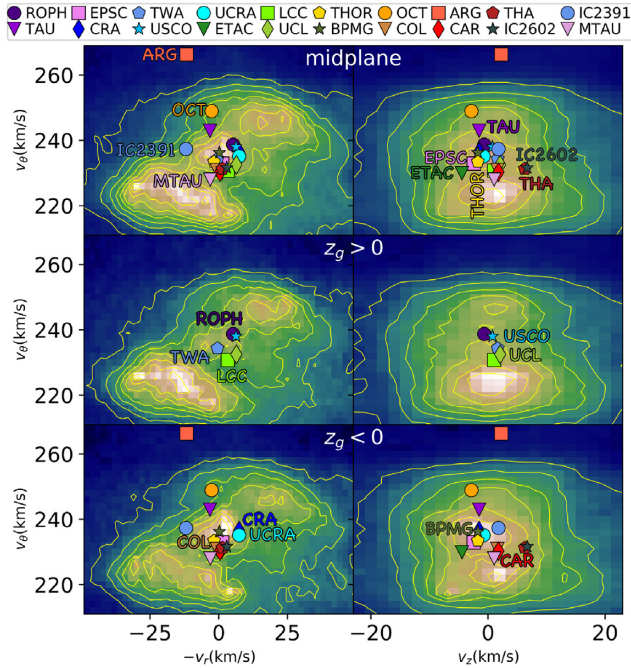
Figure 8. Stellar association velocity components plotted as points on the velocity distribution for nearby stars within 200 pc of the Sun using the *Gaia* DR2 sample. The vertical axes are the tangential velocity component v_θ in km s^{-1}. For the panels on the left, the horizontal axes are -1 times the radial velocity component $-v_R$ (adopting sign convention for the UV plane). For the panels on the right, the horizontal axes are the vertical velocity component v_z. The stellar associations tend to be located between the density peaks in the velocity distribution. The middle row is similar to the top row but only stars and associations above the Galactic plane are plotted. The bottom row is similar to the top row but only stars and associations above the Galactic plane are plotted.

Figure 9. Young stellar associations plotted as points on the vertical phase-space z_g versus v_z distribution for nearby stars within 200 pc of the Sun using the *Gaia* DR2 sample. The vertical axis is the vertical velocity component in km s^{-1}. The horizontal axis is the height above or below the Galactic plane z_g in pc. The associations older than 20 Myr are plotted with smaller point sizes. The middle panel is similar to the top one but only stars and associations with tangential velocity component $v_\theta > V_{LSR}$ are plotted. The bottom panel is similar to the top one but only stars and associations with tangential velocity component $v_\theta < V_{LSR}$ are plotted. Stellar associations seem to be associated with peaks in the vertical phase-space distribution.

corotating arm that could be the Local Spur. Many of the young stellar associations on Fig. 8 are near this under-density and have moved outward in radius after birth and so could be consistent with this interpretation, though as discussed in Sections 4.4 and 4.5, a filament with a single pattern is unlikely to account for all of them.

Quillen et al. (2018c) connected the locus separating the Coma Berenices moving group from the Sirius/Usra Major moving groups [at $(v_\theta, v_r) \sim (250, -20)$ km s^{-1}] to apocentre with the Local arm with pattern speed slower than corotation $\Omega_s = 27$ km s^{-1} kpc^{-1}. On Fig. 8, the Taurus–Auriga (TAU) star formation region is located on the opposite side of the Coma Berenices moving group peak compared to the other young associations. This would be consistent with our hypothesis that it was not born on the same filament as the others. The Octans association also seems located near this under-density; however, we suspect that it was born in an arm with an even lower pattern speed. The large difference between the v_θ of Argus and Octans associations suggests that they were not born on the same arm.

The associations that currently are above the Galactic plane (Fig. 8 middle panels) are young groups related to the Scorpius–Centaurus star formation region. The rest of the associations are currently below the Galactic plane. Other than this, we do not see any obvious trends in the comparison between stellar association and velocity distributions above and below the Galactic plane in Fig. 8.
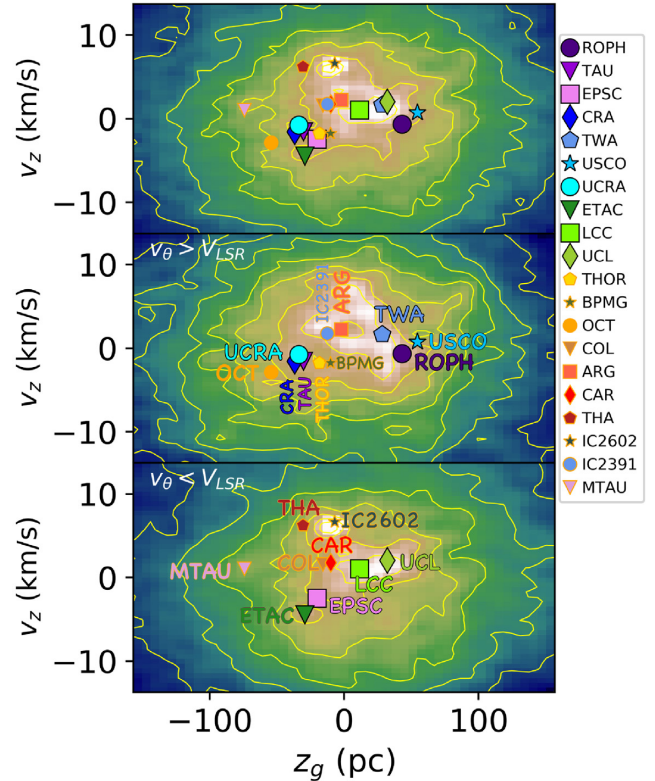
4.7 Stellar associations in comparison to the stellar vertical phase-space distribution

Phase wrapping after a tidal perturbation (e.g. Minchev et al. 2009; Candlish 2014; de la Vega et al. 2015; Antoja et al. 2018; Bland-Hawthorn et al. 2019) can affect the distribution of stars in phase space. How are the stellar associations distributed in vertical phase space or as a function of z_g and v_z? We plot in Fig. 9 the current coordinates of the stellar associations on top of the vertical phase-space distribution of stars in the solar neighbourhood. The ranges in our figure are chosen to encompass the coordinates of the stellar associations, so our plot shows only stars with orbits that remain within 200 pc of the Galactic plane. The top panel shows the distribution of stars (again from *Gaia* DR2) within 200 pc of the Sun with the young stellar associations in our sample. The middle panels plot only stars and associations that have tangential velocity $v_\theta > V_{LSR}$ and so show stars and associations that spend more time at larger galactocentric radius. The bottom panel shows stars and associations with $v_\theta < V_{LSR}$. We have checked that the stellar vertical phase-space distributions look similar if the vertical component of angular momentum is used to choose stars rather than the tangential velocity component.

The morphology of the vertical phase-space distributions in Fig. 9 shows streaks and clumps rather than a spiral that might arise from a

simple phase wrapping model (e.g. Antoja et al. 2018; Monari et al. 2018). Prior studies found that the strength of peaks in the solar neighbourhood v_θ, v_R velocity distribution is sensitive to Galactic hemisphere (Quillen et al. 2018b; Monari et al. 2018). Here, we see that the vertical phase-space distribution is sensitive to v_θ. These two phenomena are probably related. This implies that stellar motions depend on their vertical location or equivalently, as seen here, the vertical phase-space distribution is sensitive to angular momentum.

In Fig. 9, we have plotted associations younger than 20 Myr with a larger point size. This lets us compare a population of objects recently associated with the distribution and motions in the interstellar medium to those that are intermediate in age, the rest of the associations (> 20 Myr but younger than 70 Myr), and to stars in the solar neighbourhood with mean age a few Gyr. Gas dynamics differs from stellar dynamics as gas can shock, and disturbances in the gas disc will dissipate after a dynamical time. However, in all three panels in Fig. 9, the stellar associations seem to be associated with peaks in the vertical phase-space distribution. This implies that the vertical motions of gas where the stellar associations formed are related to the vertical motions of stars that are in nearly planar orbits in the Galactic disc. Perhaps the gas and stars in nearly planar orbits move vertically together.

A tidal perturbation on the disc would excite both epicyclic and vertical oscillations. Even when integrating test particles in a fixed potential, the stellar disc response can be quite complex (de la Vega et al. 2015). As stressed by Hunter & Toomre (1969), Sparke & Casertano (1988), and Darling & Widrow (2019), when a disc bends, the potential associated with the perturbation also acts on the unperturbed disc, so phase wrapping in a fixed potential (e.g. Candlish 2014; de la Vega et al. 2015) does not capture the full complexity of the stellar disc response (e.g. D'Onghia et al. 2016). The clumps seen in the vertical phase-space distribution could be showing a rippled disc that was perturbed in the past (Minchev et al. 2009; Quillen et al. 2009; Chakrabarti et al. 2011; Purcell et al. 2011; Gómez et al. 2013; D'Onghia et al. 2016; Bland-Hawthorn et al. 2019; Darling & Widrow 2019). Recent tidal perturbations, such as the interaction of the Antlia 2 dwarf galaxy, on a nearly co-planar orbit with the Milky Way (Chakrabarti et al. 2019) or the Sagittarius dwarf Galaxy (e.g. Laporte et al. 2019), would also leave visible traces in the gas distribution at present day.

In the *Gaia* DR2 sample, Antoja et al. (2018) discovered a spiral in the vertical phase-space distribution of stars in the solar neighbourhood by plotting the distribution of stars as a function of z_g and v_z. The phase-space spiral (Antoja et al. 2018; Bland-Hawthorn et al. 2019; Laporte et al. 2019) is present at larger scales in both v_z and z_g than we show in Fig. 9. The ranges in our figure are chosen to encompass the coordinates of the stellar associations; however, the innermost edge of the spiral seen by Antoja et al. (2018) is at about $|v_z| \sim 20$ km s^{-1} and $|z_g| \sim 250$ pc and would lie outside our plot.

5 SUMMARY AND DISCUSSION

In this study, we have used recent compilations of membership, space motions, distances and ages of young (less than 70 Myr old) clusters, stellar associations, and star formation regions near the Sun to estimate their birth locations. Our works build upon efforts of hundreds of prior observational and statistical studies of stars (e.g. Eggen 1983; de la Reza et al. 1989; de Zeeuw et al. 1999; Mamajek et al. 1999; Jayawardhana 2000; Binks et al. 2015; Mamajek 2016; Pecaut & Mamajek 2016; Gagné et al. 2018a). Our backwards orbit integrations are done in a gravitational potential that is an approximation to the Galactic gravitational potential near

the Sun. This potential is static, separable, and axisymmetric, and matches recent estimates for the LSR, the rotation curve slope, and the vertical acceleration as a function of height above the Galactic plane.

Most of the stellar associations were born within the radius of the Sun and have moved out to the solar neighbourhood where they are now found. The Octans and Argus associations are exceptions as they were born at larger galactocentric radius than the Sun. One way to account for these trends is with a spiral structure model where nearby spiral features have different pattern speeds. A spiral arm with pattern speed that is higher than $\Omega_\odot$ places associations currently on the trailing side of their birth arm. In this case, *N*-body simulations of flocculent approximately corotating spiral structure (Grand et al. 2012) and shock models can predict outwards radial motion after birth. Alternatively, the associations that moved outward were born on the trailing side of a corotating spiral arm that increased their angular momentum through its gravitational torque (Kawata et al. 2014). Other scenarios, such as involving tidally excited spiral structure or spurs and armlets extending from strong arms, might also account for the radial motions after birth (e.g. Dobbs & Pringle 2010).

Variations in birth heights of the stellar associations suggest that they were born in a corrugated disc of molecular clouds, similar to that inferred from the current filamentary molecular cloud distribution (Alves et al. 2020) and extinction maps (Rezaei et al. 2018; Green et al. 2019; Lallement et al. 2019). Maximum vertical heights reached above or below the galactic plane are high for the youngest and oldest stellar associations but only about 30 pc for the 20–30 Myr older associations such as the β Pictoris moving group. This implies that there were spatial variations in the amplitudes of the vertical motions in the molecular cloud distributions in the recent past.

We examined birth locations in frames rotating at different pattern speeds. Multiple arms with different pattern speeds and different heights seem required to account for the stellar association birth locations, suggesting that spiral arms or molecular cloud filaments exhibited transient behaviour in the past 50 Myr near the Sun. The 45-Myr-old Columba (COL), Tucana–Horologium (THA), and Carina (CAR) associations have similar birth heights and could have been born on the same filament that is associated with the 'Split' or 'Vul' extinction features with a pattern speed of ~30 km s^{-1} kpc^{-2}. The Argus and Octans associations could have been born on an arm with pattern speed of ~26 km s^{-1} kpc^{-2} that is now associated with the Vela C molecular cloud. The younger associations (less than 25 Myr old) could have been born on nearly corotating filaments at different heights.

We find that the stellar associations are located in between peaks in the v_θ, v_R stellar velocity distribution for stars in the solar neighbourhood. This supports the hypothesis that the dips in the velocity distribution are associated with orbits that touch nearby spiral density features (Quillen et al. 2018c). In contrast, stellar associations seem to be located near peaks in the vertical phase-space distribution (z_g, v_z), suggesting that the gas in which stellar associations are born moves together with the the low-velocity dispersion disc stars.

Ongoing efforts are discovering new stellar associations (e.g. Kounkel & Covey 2019; Meingast et al. 2019; Gagné et al. in preparation; Kounkel, Covey & Stassun 2020), substructure in known star formation regions and associations (e.g. Kos et al. 2019; Tian 2020), improving upon the accuracy of membership age distributions, and position and velocity measurements (e.g. Ujjwal et al. 2020). A backwards integration study can be redone in the future with

additional and better measurements and in time-dependent and non-axisymmetric potential models. More distant stellar associations may reveal patterns of star formation in the Local and other arms. Lastly, improved dissection of *N*-body simulations that include gas dynamics and star formation could help differentiate between potential spiral arm models and the nature of the vertical motions seen in the stars, gas, and stellar associations in the solar neighbourhood.

ACKNOWLEDGEMENTS

DATA AVAILABILITY

New data generated are incorporated into the article.

REFERENCES

Alves J. et al., 2020, Nature, 578, 237
Anderson L. D., Wenger T. V., Armentrout W. P., Balser D. S., Bania T. M., 2019, ApJ, 871, 145
Antoja T. et al., 2018, Nature, 561, 360
Baba J., Saitoh T. R., Wada K., 2013, ApJ, 763, 46
Baba J., Morokuma-Matsui K., Miyamoto Y., Egusa F., Kuno N., 2016, MNRAS, 460, 2472
Barrado y Navascués D., Stauffer J. R., Jayawardhana R., 2004, ApJ, 614, 386
Barros D. A., Lépine J. R. D., Dias W. S., 2016, A&A, 593, A108
Bell C. P. M., Mamajek E. E., Naylor T., 2015, MNRAS, 454, 593
Bennett M., Bovy J., 2019, MNRAS, 482, 1417
Bertin G., Lin C. C., Lowe S. A., Thurstans R. P., 1989, ApJ, 338, 104
Binks A. S., Jeffries R. D., Maxted P. F. L., 2015, MNRAS, 452, 173
Binks A. S. et al., 2020, MNRAS, 491, 215
Bland-Hawthorn J. et al., 2019, MNRAS, 486, 1167
Bouy H., Alves J., 2015, A&A, 584, A26
Buta R. J., Byrd G. G., Freeman T., 2003, AJ, 125, 634
Candlish G. N., Smith R., Fellhauer M., Gibson B. K., Kroupa P., Assmann P., 2014, MNRAS, 437, 3702
Chakrabarti S., Blitz L., 2009, MNRAS, 399, L118
Chakrabarti S., Laughlin G., Shu F. H., 2003, ApJ, 596, 220
Chakrabarti S., Bigiel F., Chang P., Blitz L., 2011, ApJ, 743, 35
Chakrabarti S., Chang P., Price-Whelan A. M., Read J., Blitz L., Hernquist L., 2019, ApJ, 886, 67
Comparetta J., Quillen A. C., 2012, preprint (arXiv:1207.5753)
Crundall T. D., Ireland M. J., Krumholz M. R., Federrath C., Zerjal M., Hansen J. T., 2019, MNRAS, 489, 3625
D'Onghia E., Madau P., Vera-Ciro C., Quillen A., Hernquist L., 2016, ApJ, 823, 4
Darling K., Widrow L. M., 2019, MNRAS, 484, 1050
de la Reza R., Jilinski E., Ortega V. G., 2006, AJ, 131, 2609
de Zeeuw P. T., Hoogerwerf R., de Bruijne J. H. J., Brown A. G. A., Blaauw A., 1999, AJ, 117, 354
Debattista V. P., Moore B., Quinn T., Kazantzidis S., Maas R., Mayer L., Read J., Stadel J., 2008, ApJ, 681, 1076
Deg N., Widrow L. M., Randriamampandry T., Carignan C., 2019, MNRAS, 486, 5391
Dehnen W., 1998, AJ, 115, 2384
Dehnen W., 1999, AJ, 118, 1190
de la Reza R., Torres C. A. O., Quast G., Castilho B. V., Vieira G. L., 1989, ApJ, 343, L61
de la Vega A., Quillen A. C., Carlin J. L., Chakrabarti S., D'Onghia E., 2015, MNRAS, 454, 933
Dias W. S., Lepine J. R. D., 2005, ApJ, 629, 825
Dias W. S., Monteiro H., Lepine J. R. D., Barros D. A., 2019, MNRAS, 486, 5726
Dobbie P. D., Lodieu N., Sharp R. G., 2010, MNRAS, 409, 1002
Dobbs C. L., Pringle J. E., 2010, MNRAS, 409, 396
Eggen O. J., 1983, MNRAS, 204, 377
Elias F., Alfaro E. J., Cabrera-Cano J., 2006, AJ, 132, 1052
Fleming G. D., Kirk J. M., Ward-Thompson D., Pattle K. M., 2020, ApJ, preprint (arXiv:1904.06980), in press
Flynn C., Holmberg J., Portinari L., Fuchs B., Jahreiss H., 2006, MNRAS, 372, 1149
Gagné J., Faherty J. K., 2018, ApJ, 862, 138
Gagné J. et al., 2018a, ApJ, 856, 23
Gagné J., Roy-Loubier O., Faherty J. K., Doyon R., Malo L., 2018b, ApJ, 860, 43
Gagné J., Faherty J. K., Mamajek E. E., 2018c, ApJ, 865, 136
Gaia Collaboration, 2018, A&A, 616, A11
Galli P., Bouy H., Olivares J., Miret-Roig N., Sarro L., Barrado D., Berihuete A., Brandner W., 2020, A&A, 634, A98
Gennaro M., Moroni P. G. P., Tognelli E., 2010, MNRAS, 420, 986
Gómez F. A., Minchev I., O'Shea B. W., Beers T. C., Bullock J. S., Purcell C. W., 2013, MNRAS, 429, 159
Gould B. A., 1874, Am. J. Sci. Series, 38, 325
Grand R. J. J., Kawata D., Cropper M., 2012, MNRAS, 421, 1529
Grand R. J. J., Bovy J., Kawata D., Hunt J. A. S., Famaey B., Siebert A., Monari G., Cropper M., 2015, MNRAS, 453, 1867
GRAVITY Collaboration, 2018, A&A, 615, L15
Green G. M., Schlafly E. F., Zucker C., Speagle J. S., Finkbeiner D. P., 2019, ApJ, 887, 93
Herschel J. F. W., 1847, Results of Astronomical Observations Made During the Years 1834, 5, 6, 7, 8, at the Cape of Good Hope; Being the Completion of a Telescopic Survey of the Whole Surface of the Visible Heavens, Commenced in 1825. Smith, Elder and Company, London
Holmberg J., Flynn C., 2000, MNRAS, 313, 209
Holmberg J., Flynn C., 2004, MNRAS, 352, 440
Hunter C., Toomre A., 1969, ApJ, 155, 747
Jayawardhana R., 2000, Science, 288, 64
Johnson D. R. H., Soderblom D. R., 1987, AJ, 93, 864
Kawata D., Hunt J. A. S., Grand R. J. J., Pasetto S., Cropper M., 2014, MNRAS, 443, 2757
Kos J. et al., 2019, A&A, 631, 166
Kounkel M., Covey K., 2019, AJ, 158, 122
Kounkel M., Covey K., Stassun K. G., 2020, preprint (arXiv:2004.07261)
Krause M. G. H. et al., 2020, Space Sci. Rev., 216, 64
Lallement R., Babusiaux C., Vergely J. L., Katz D., Arenou F., Valette B., Hottier C., Capitanio L., 2019, A&A, 625, A135
Laporte C. F. P., Minchev I., Johnston K. V., Gómez F. A., 2019, MNRAS, 485, 3134
Levine E. S., Blitz L., Heiles C., 2006a, Science, 312, 1773
Levine E. S., Blitz L., Heiles C., 2006b, ApJ, 643, 881
Li C., Zhao G., Yang C., 2019, ApJ, 872, 205
Lin C. C., Shu F. H., 1966, Proc. Natl. Acad. Sci. USA, 55, 229
Lindblad P. A. B., Lindblad P. O., Athanassoula E., 1996, A&A, 313, 65
Malo L., Doyon R., Lafreniere D., Artigau E., Gagne J., Baron F., Riedel A., 2013, ApJ, 762, 88
Mamajek E. E., 2016, in Kastner J. H., Stelzer B., Metchev S. A., eds, Proc. IAU Symp. 314, Young Stars & Planets Near the Sun, Cambridge University Press, Cambridge, p. 21
Mamajek E. E., Lawson W. A., Feigelson E. D., 1999, ApJ, 516, L77
McGaugh S. S., 2019, ApJ, 885, 87
McKee C. F., Parravano A., Hollenbach D. J., 2015, ApJ, 814, 13

Meingast S., Alves J., Furnkranz V., 2019, A&A, 622, 13
Minchev I., Quillen A. C., Williams M., Freeman K. C., Nordhaus J., Siebert A., Bienayme O., 2009, MNRAS, 396, L56
Miret-Roig N., Antoja T., Romero-Gomez M., Figueras F., 2018, A&A, 615, A51
Monari G. et al., 2018, Res. Notes Am. Astron. Soc., 2, 32
Mróz P. et al., 2019, ApJ, 870, L10
Murphy S. J., Lawson W. A., 2015, MNRAS, 447, 1267
Murphy S. J., Lawson W. A., Bessell M. S., 2013, MNRAS, 435, 1325
Naoz S., Shaviv N. J., 2007, New Astron., 12, 410
Pecaut M., Mamajek E. E., 2016, MNRAS, 461, 794
Perrot C. A., Grenier I. A., 2003, A&A, 404, 519
Pettitt A. R., Dobbs C. L., Acreman D. M., Bate M. R., 2015, MNRAS, 449, 3911
Pettitt A. R., Tasker E. J., Wadsley J. W., Keller B. W., Benincasa S. M., 2017, MNRAS, 468, 4189
Platais I., Kozhurina-Platais V., van Leeuwen F., 1998, AJ, 116, 2423
Prada J., Forero-Romero J. E., Grand R. J. J., Pakmor R., Springel V., 2019, MNRAS, 490, 4877
Purcell C. W., Bullock J. S., Tollerud E. J., Rocha M., Chakrabarti S., 2011, Nature, 477, 301
Quillen A. C., 2002, AJ, 124, 924
Quillen A. C., Minchev I., Bland-Hawthorn J., Haywood M., 2009, MNRAS, 397, 1599
Quillen A. C., Dougherty J., Bagley M. C., Minchev I., Comparetta J., 2011, MNRAS, 417, 762
Quillen A. C., Nolting E., Minchev I., De Silva G., Chiappini C., 2018a, MNRAS, 475, 4450
Quillen A. C. et al., 2018b, MNRAS, 478, 228
Quillen A. C. et al., 2018c, MNRAS, 480, 3132
Reid M. J. et al., 2014, ApJ, 783, 130
Reid M. J. et al., 2019, ApJ, 885, 131
Reipurth B., ed., 2008, ASP Conf. Ser. Vol. I, Handbook of Star-forming Regions, Vol. I:The Northern Sky. Astron. Soc. Pac., San Francisco
Rezaei Kh. S., Bailer-Jones C. A. L., Hogg D. W., Schultheis M., 2018, A&A, 618, A168
Riedel A. R., Blunt S. C., Lambrides E. L., Rice E. L., Cruz K. L., Faherty J. K., 2017, AJ, 153, 95
Robin A. C., Reylé C., Derrière S., Picaud S., 2003, A&A, 409, 523
Schönrich R., Binney J., Dehnen W., 2010, MNRAS, 403, 1829
Sellwood J. A., Carlberg R. G., 1984, ApJ, 282, 61
Sellwood J. A., Carlberg R. G., 2014, ApJ, 785, 137
Shetty R., Vogel S. N., Ostriker E. C., Teuben P. J., 2007, ApJ, 665, 1138
Shu F. H., 2016, ARA&A, 54, 667
Sparke L. S., Casertano S., 1988, MNRAS, 234, 873
Tian H.-J., 2020, preprint (arXiv:2005.12265)
Toomre A., 1981, in Fall S., Lynden-Bell D., eds, Vol. Proceedings of a NATO Advanced Study Institute at the Institute of Astronomy and Clare College, Cambridge, August 3-15, 1980, The structure and evolution of normal galaxies. Cambridge Univ. Press, Cambridge and New York, p. 111
Ujjwal K., Kartha S. S., Mathew B., Manoj P., Narang M., 2020, AJ, 159, 166
Wada K., Baba J., Saitoh T. R., 2011, ApJ, 735, 1
Wilking B. A., Gagné M., Allen L. E., 2008, in Reipurth B., ed, ASP Conf. Ser. Vol. 5, Handbook of Star Forming Regions, Volume II, The Southern Sky. Astron. Soc. Pac., San Francisco, p. 351
Wright N. J., Mamajek E. E., 2018, MNRAS, 476, 381
Xu Y. et al., 2016, Sci. Adv., 2, e160087
Xu Y. et al., 2018, A&A, 616, L15
Zari E., Hashemi H., Brown A. G. A., Jardine K., de Zeeuw P., 2018, A&A, 620, A172
Zucker C., Speagle J. S., Schlafly E. F., Green G. M., Finkbeiner D. P., Goodman A., Alves J., 2020, A&A, 633, A51
Zuckerman B., 2019, ApJ, 870, 27
Zuckerman B., Song I., 2004, ARA&A, 42, 685

SUPPORTING INFORMATION

Supplementary data are available at *MNRAS* online.

movie3D.mpg

Please note: Oxford University Press is not responsible for the content or functionality of any supporting materials supplied by the authors. Any queries (other than missing material) should be directed to the corresponding author for the article.

This paper has been typeset from a TEX/LATEX file prepared by the author.